CHAPTER 3

RESULTS AND DISCUSSION

This chapter details the formulation and systematic evaluation of biopolymeric complexes designed for controlled oral delivery of hypoglycaemic agents (curcumin and α-lipoic acid). It demonstrates how fine-tuning the concentrations of crosslinker and filler can enhance drug encapsulation, modulate pH-responsive release, and safely improve glucose uptake in diabetic cell models.

3.1. CHITOSAN-ALGINATE COMPLEX FOR THE CONTROLLED DELIVERY OF α-LIPOIC ACID: MODULATION BY MONTMORILLONITE AND GLUTARALDEHYDE

3.1.1. Process yields, drug encapsulation efficiency, and drug loading efficiency

The process yield was calculated using the formula provided in section 2.2.7 (Chapter 2). Table 3.1 shows the yield, encapsulation efficiency, and drug loading efficiency results for various polymer systems developed for delivering LA, illustrating the impact of varying MMT and GA concentrations on the properties of the Ch/Alg complex. Variation in MMT concentration had a minimal effect on yield (%), which decreased with an increase in crosslinker concentration. This might be due to loss during isolation. Complexes crosslinked without MMT demonstrated higher encapsulation and drug loading efficiency than those with MMT. As the MMT content increased, the encapsulation efficiency and drug loading efficiency decreased. This effect can be attributed to the interaction between the –OH groups of MMT's silicate layers, the –OH and $–NH_2$ groups in chitosan, and the –COOH groups of alginate, causing the polymer chains to extend. The silicate layers in MMT restrict the free movement of intercalated polymer chains, forming a porous structure during dehydration, with multiple small channels running from the interior to the outer surface of the complex. As a result, part of the drug could diffuse out of the complex into the surrounding medium, lowering both encapsulation efficiency and drug loading efficiency [1, 2]. The absence of MMT layers in the MMT-free crosslinked complex eliminated the hindrance observed in those with MMT. Additionally, incorporating MMT may reduce the available space for drug accommodation, leading to a decline in encapsulation and loading efficiency. Similarly, as the concentration of glutaraldehyde (GA), a crosslinker, increased, the encapsulation efficiency of the complex decreased. GA might restrict the free movement of polymer chains, promoting the formation of a porous structure. The drug could migrate through these pores or channels from the complex's interior to the surrounding medium. Moreover, interactions with the crosslinker may cause the polymer to become more rigid and compact, reducing the internal free volume. Consequently, both encapsulation and drug loading efficiency decreased. As expected, the combined effect of both MMT and glutaraldehyde decreased the encapsulation and drug loading efficiency.

Table 3.1. Effect of GA and MMT on properties of Lipoic Acid loaded Chitosan-Alginate complex*

Sample Code(a)	**Chitosan % w/v (amount in g in 50 mL water)**	**Alginate % w/v (amount in g in 50 mL water)**	**Amount of crosslinker, % v/w (in µL)**	**Amount of MMT clay, % w/w w.r.t. CA (g in 50mL water)**	**Process Yield (%)**	**Encapsulation Efficiency (%)**	**Drug Loading Efficiency (%)**
CA	0.1 (0.05)	0.3 (0.15)	0	0	70.4 (±0.03)	64.2 (±0.04)	49.3 (±0.01)
CA/GA1	0.1 (0.05)	0.3 (0.15)	2.5 (5)	0	68.2 (±0.03)	61.9 (±0.02)	46.8 (±0.03)
CA/GA2	0.1 (0.05)	0.3 (0.15)	5 (10)	0	69.7 (±0.02)	60.4 (±0.05)	42.9 (±0.05)
CA/GA3	0.1 (0.05)	0.3 (0.15)	7.5 (15)	0	67.1 (±0.03)	57.8 (±0.02)	38.2 (±0.05)
CA/M1	0.1 (0.05)	0.3 (0.15)	0	0.3 (0.06)	70.8 (±0.02)	62.8 (±0.05)	40.6 (±0.04)
CA/M2	0.1 (0.05)	0.3 (0.15)	0	1.2 (0.24)	71.4 (±0.01)	60.2 (±0.04)	38.2 (±0.01)
CA/M3	0.1 (0.05)	0.3 (0.15)	0	4.8 (0.96)	71 (±0.02)	61.4 (±0.03)	38.9 (±0.04)
CA/GA2/M2	0.1 (0.05)	0.3 (0.15)	5 (10)	1.2 (0.24)	68.46 (±0.02)	55.2 (±0.01)	34.5 (±0.02)

Lipoic Acid = 0.01g, Tween 80 = 0.015 mL.

(a) In the sample code, Chitosan-Alginate PEC, glutaraldehyde, and MMT are represented by “CA,” “GA,” and “M,” respectively.

*Each value and the standard deviation in parentheses represent the average of five readings.

3.1.2. *In vitro* drug release studies

The drug release study for the complex was conducted at two different pH levels, 1.2 and 7.4, throughout 1 to 50 hours, as shown in the figure below. The cumulative release (%) of LA from the complex was found to be dependent on pH. Drug release was higher in the alkaline medium compared to the acidic medium. In an acidic medium, the amino groups of chitosan became protonated, thereby enhancing interaction with the carboxylate groups of Na-Alg to form a compact structure. Hence, the rate of swelling and the rate of LA release would decrease. Further, LA's protection was likely also due to the stronger retention by the tightly bound alginate network that forms at low pH in the acidic environment. In contrast, in an alkaline medium, the deprotonation of chitosan decreased the interaction between chitosan and Na-Alg, thereby facilitating swelling to occur more readily. This would accelerate the release of LA. Additionally, in the alkaline medium, the breakdown of hydrogen bonding between the polymer and LA promoted drug release, resulting in higher cumulative release. The significant swelling of the complex at alkaline pH allowed easier solvent access to the drug within the polymer matrix, enhancing contact and thus enabling higher drug release [3, 4].

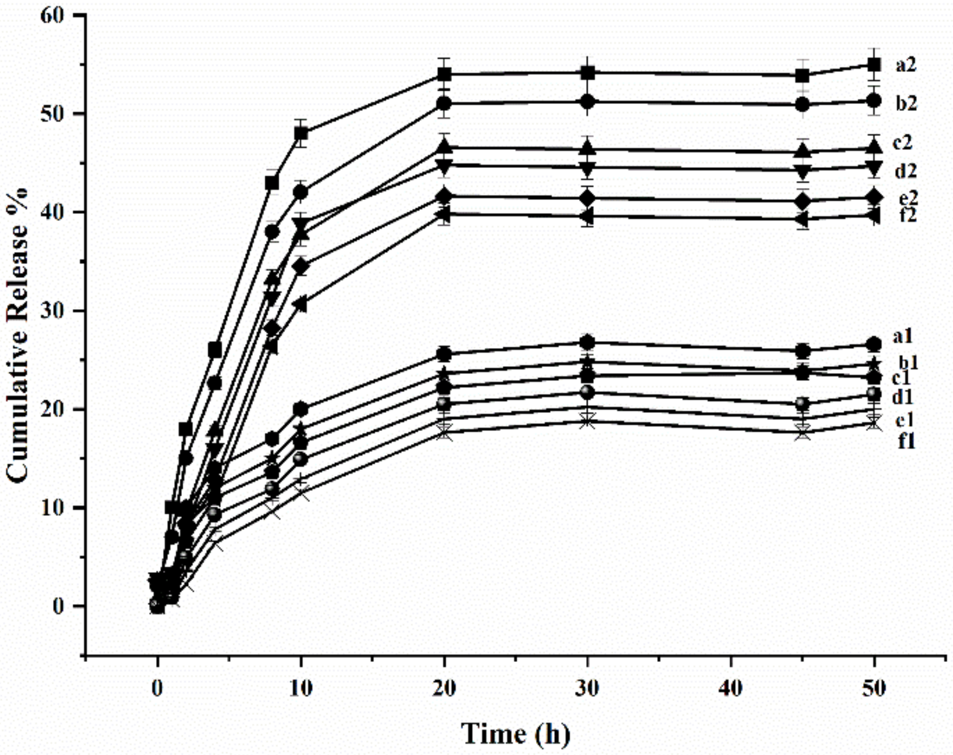

Figure 3.1. Effect of variation of concentration of GA and MMT on the percentage cumulative release of LA from the drug-loaded complex at pH 7.4 {(a2)CA, (b2)CA/M1, (c2)CA/M3, (d2) CA/GA1, (e2) CA/GA3, (f2)CA/GA2/M2} and pH 1.2{(a1) CA, (b1) CA/M1, (c1) CA/M3, (d1) CA/GA1, (e1) CA/GA3, (f1)CA/GA2/M2}

The data indicated that LA’s cumulative release (%) decreased as the MMT content and time increased. The silicate layers of MMT acted as a barrier, preventing solvent molecules from entering the complex. The higher the concentration of MMT, the higher the resistance. Consequently, the ability of solvent particles to reach the LA molecules encapsulated in the complex decreased, and thus, it became restricted. The drug release increased up to a specific time and then remained almost unchanged throughout the period. Over time, the swelling of the complex increases, allowing more solvent particles to reach the drug molecule and facilitate the release of LA from the complex [2]. The data indicated that LA’s cumulative release (%) decreased as the concentration of GA increased. This was attributed to the complex's higher crosslinking density at higher GA concentrations.

Increased GA concentration produces a more crosslinked complex, reducing solvent access to the LA molecule encapsulated in the polymer complex and decreasing its release [5]. Therefore, there is a decrease in the cumulative release of LA.

3.1.3. Characterisation

3.1.3.1. Fourier transform infrared spectroscopy

In the FTIR spectrum, curve (a) corresponds to the spectrum of sodium alginate. Key peaks include a broad band at 3452 cm^{-1}, attributed to O-H stretching, indicative of the hydroxyl groups in the polysaccharide structure. The band at 1603 cm^{-1} is associated with C=O stretching from the carboxylate groups of alginate, while the peak at 2920 cm^{-1} corresponds to C-H stretching. The band observed at 1396 cm^{-1} is due to COO^{-} stretching, and a strong band at 1021 cm^{-1} is linked to C-C and -OOC bond vibrations. A peak at 816 cm^{-1} is also assigned to Na–O bonding, a characteristic feature of sodium alginate [6].

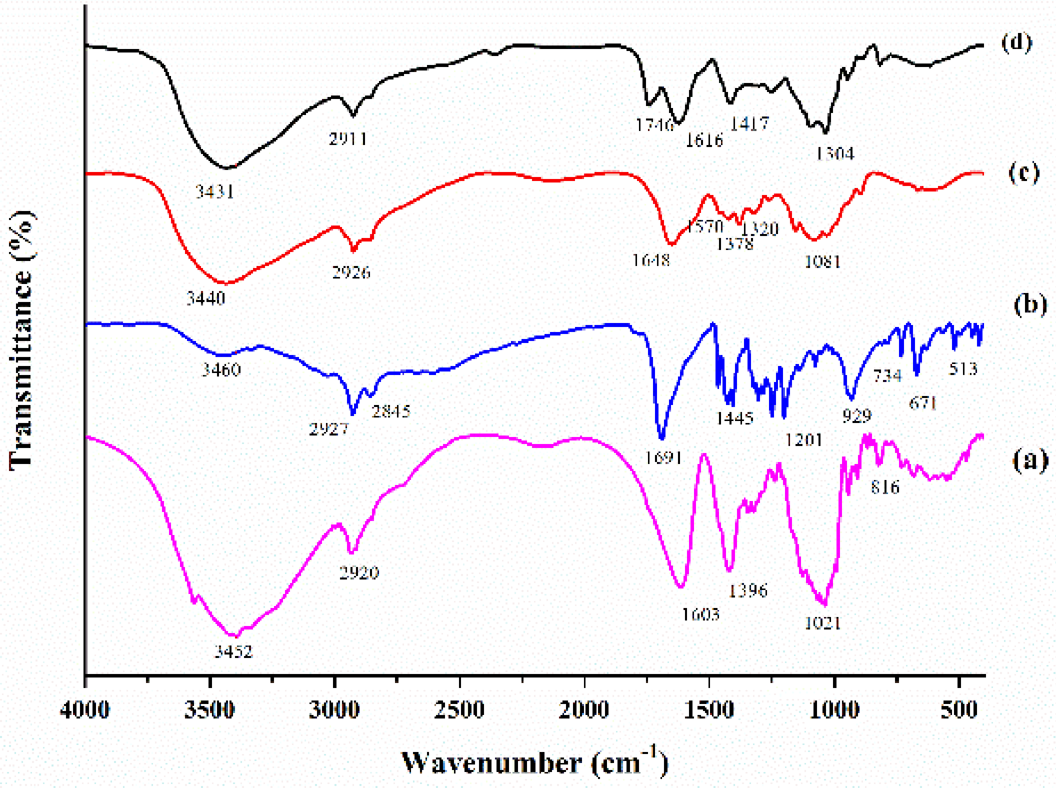

Figure 3.2 FTIR spectra of (a)Alginate, (b) Lipoic Acid, (c) Chitosan, (d) CA

Curve (b) shows the spectrum of lipoic acid. A broad absorption band around 3460 cm^{-1} is assigned to O–H stretching. Peaks at 1691 cm^{-1} and 929 cm^{-1} are attributed to C–O stretching and out-of-plane O–H bending of the carboxylic acid group. The region between 2927–2845 cm^{-1} displays weaker absorption due to overlapping C–H and O–H stretching bands. Peaks at 1445 cm^{-1} and 734 cm^{-1} are associated with CH_2 scissoring and rocking vibrations, while the region between 1445–1201 cm^{-1} is linked to a combination of C–O stretching, O–H bending, and CH_2 twisting. Additionally, peaks at 671 cm^{-1} and 513 cm^{-1} correspond to C–S and S–S stretching vibrations [7].

Curve (c) represents the FTIR spectrum of chitosan. The O-H stretching band is located at 3440 cm^{-1}, while a peak at around 1648 cm^{-1} is due to the amide I band, indicative of the C=O stretching in chitosan's structure. A peak at 1570 cm^{-1} corresponds to N-H bending, confirming the presence of amino groups. The band at 2926 cm^{-1} is associated with C-H stretching. The peaks at around 1378 cm^{-1} and 1320 cm^{-1} are associated with CH_2 bending and amide III bands, respectively, and the peak at 101 cm^{-1} corresponds to the C-O-C stretching vibration characteristic of the glycosidic linkages in chitosan.

Curve (d) represents the FTIR spectrum of the lipoic acid-loaded chitosan-alginate complex. Several significant changes can be observed in this spectrum compared to the individual spectra of sodium alginate, chitosan, and lipoic acid. The OH stretching band shifted from 3452cm^{-1} in Na alginate and 3440 cm^{-1} in chitosan to 3431 cm^{-1}, indicating hydrogen bond formation between the OH and NH_2 groups of chitosan and the C=O and OH groups of Na alginate. Peaks at 1691 cm^{-1} and 929 cm^{-1}, corresponding to C–O stretching and out-of-plane OH bending of lipoic acid, were reduced in intensity or disappeared, indicating interaction with chitosan and alginate. The carbonyl (C=O) band shifted from 1603 cm^{-1} in Na alginate to 1616 cm^{-1} due to the presence of chitosan, while the Na–O peak of sodium alginate remained. A new peak at 1746 cm^{-1}, corresponding to the asymmetric stretching of the COO group, indicates interaction between the carboxyl group of alginate and the amino group of chitosan, likely forming amide linkages. The overall reduction in peak intensity and shifts in wavenumbers indicate improved dispersion of lipoic acid within the chitosan-alginate complex. These spectral changes suggest successful interactions between the components, such as alginate, chitosan, and lipoic acid, indicating the formation of a stable biopolymeric complex.

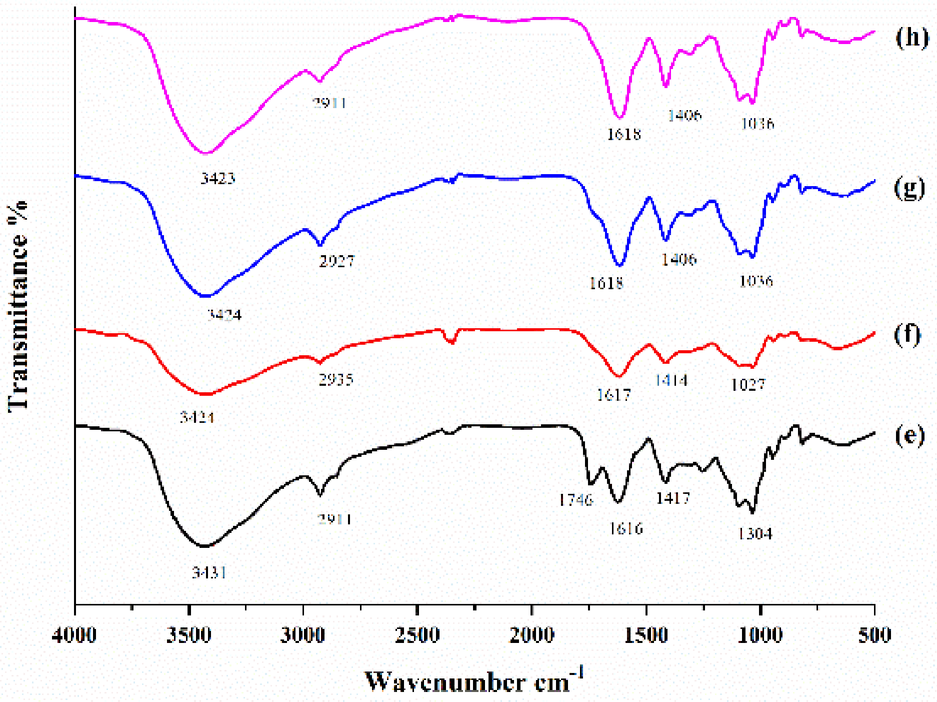

Figure 3.3. FTIR spectra of (e) CA, (f) CA/GA1, (g) CA/GA3, (h) CA/GA2/M2

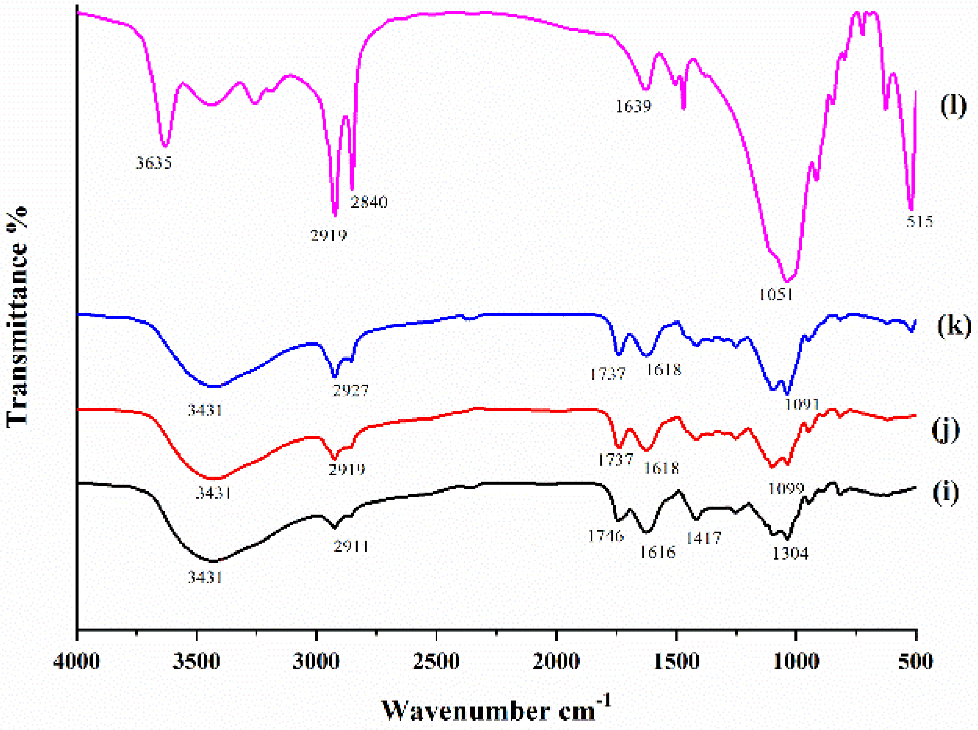

Figure 3.4. FTIR spectra of (i) CA (j) CA/M1, (k) CA/M3, (l) MMT

In the spectra of glutaraldehyde-crosslinked samples, the hydroxyl peak for crosslinker-free complexes appeared at 3431 cm^{-1} and shifted to a lower wavenumber of 3424 cm^{-1}. The intensity of the peak corresponding to the -COO stretching at 1746 cm^{-1} also showed a shift. In the spectra of MMT, peaks were observed at 3635 cm^{-1}, 1639 cm^{-1}, and in the range 1051-544 cm^{-1}, corresponding to -OH stretching, -OH bending, and oxide bends of metals like Si, Al, and Mg.

For the MMT-loaded samples, the peak at 1746 cm^{-1} in chitosan shifted to 1737 cm^{-1} for the complex. In the spectrum of the glutaraldehyde crosslinked lipoic acid-loaded chitosan-MMT-alginate system, the characteristic peaks of chitosan, alginate, MMT, and lipoic acid were present, although their intensities were reduced. These observations indicate enhanced MMT and lipoic acid dispersion within the chitosan-alginate complex.

3.1.3.2. X-ray diffraction study

Lipoic acid (LA) exhibits distinct sharp peaks at 2θ = 23° and 2θ = 19°, which indicate its crystalline nature.

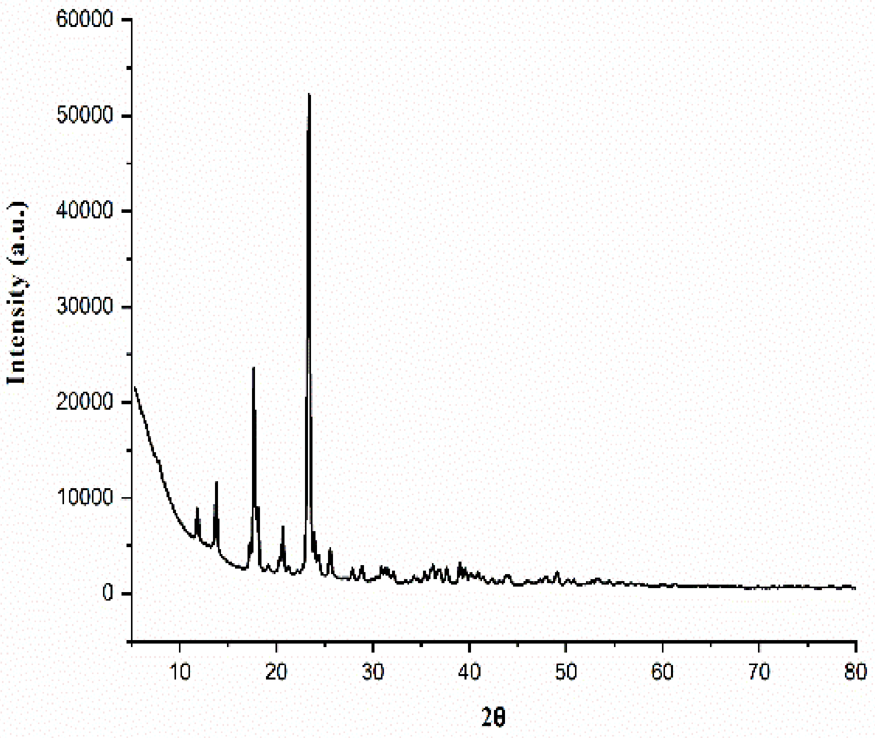

Figure 3.5. XRD Pattern of Lipoic Acid

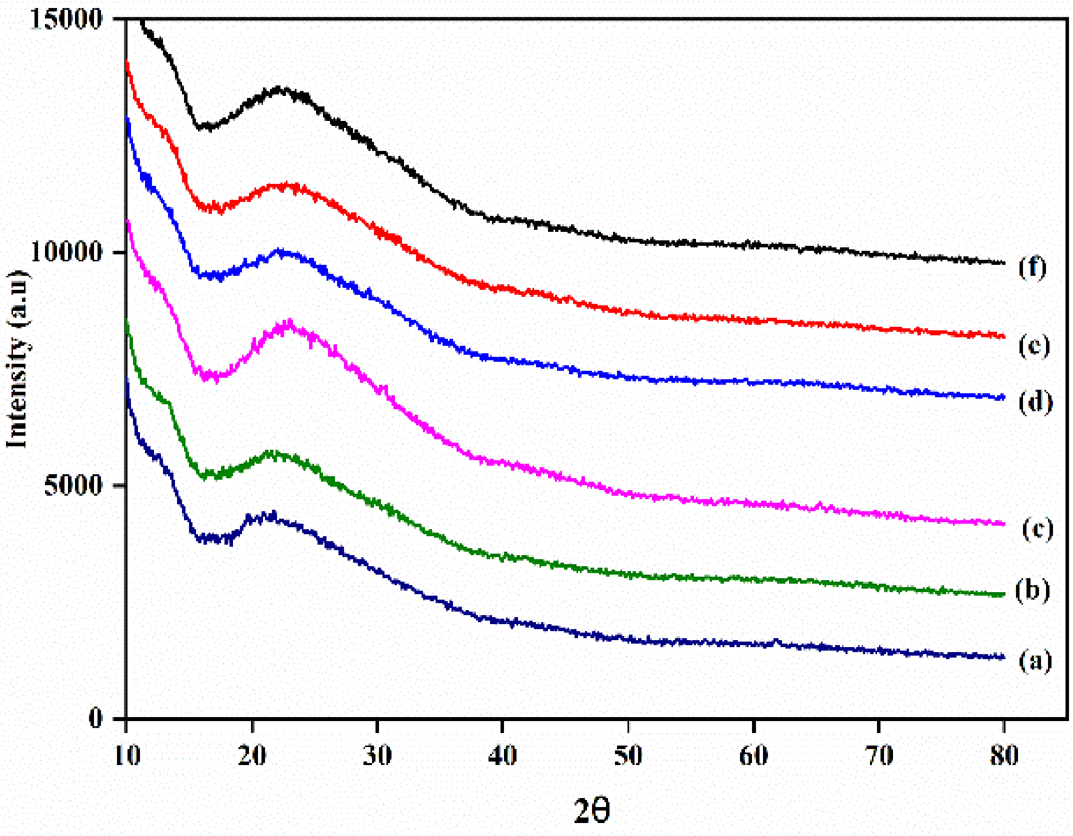

Figure 3.6. XRD patterns of (a) CA, (b) CA/GA1, (c) CA/GA3, (d) CA/M1, (e) CA/M3, (f) CA/GA2/M2

The CA system's diffractogram showed a distinct broad peak at 2θ = 21°, with a minor right shift on the addition of crosslinker and MMT. The characteristic peaks for lipoic acid disappeared in the diffractogram of the drug-loaded complex. This suggests the formation of an amorphous region, likely due to the suppression of the drug's crystallisation within the confinement of the polymer matrix [8, 9]. This also indicates the molecular-level dispersion of LA within the complex and the amorphous or disordered crystalline nature of LA in the polymer matrix. The transition to an amorphous state (as suggested by the disappearance of these peaks in Figure 3.6 for drug-loaded formulations) can significantly enhance the drug’s solubility and bioavailability [10].

3.1.3.3. Scanning electron microscope (SEM) study

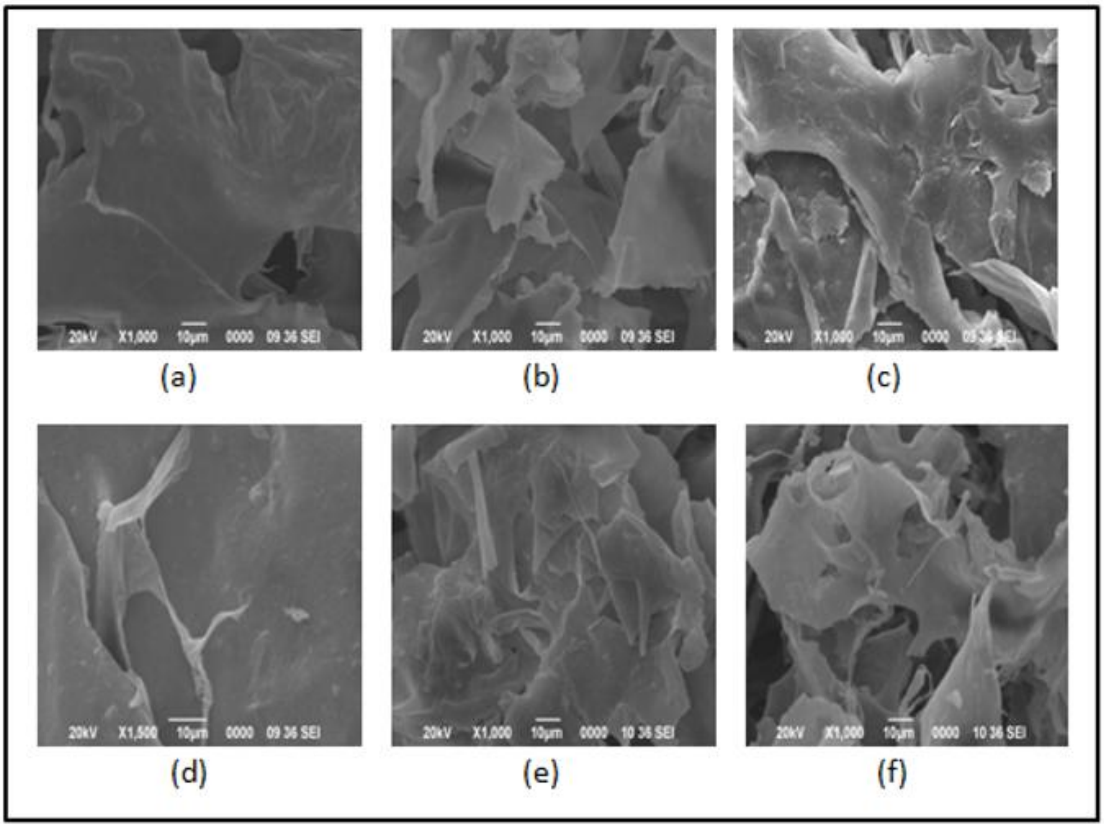

Figure 3.7. SEM micrographs of (a) CA, (b) CA/GA1, (c) CA/GA3, (d) CA/M1, (e) CA/M3, (f) CA/GA2/M2

SEM analysis examined the surface morphologies of drug-loaded polyelectrolyte complexes with varying concentrations of MMT and crosslinker. The surface of CA appeared smooth. The surface smoothness decreased gradually with increased crosslinker concentration (Figure 3.7: b and c), indicating increased interaction between the CA complex and GA. An increase in the concentration of GA has resulted in densification, as evident in the SEM images (Figure 3.7: b, c, f). The inclusion of MMT (0.3%) (Figure 3.7: d) did not much change the surface morphology compared to the CA complex. However, a further increase in MMT (4.8%) (Figure 3.7: e) has resulted in a rougher, more textured surface, suggesting an agglomeration of MMT. The combined inclusion of MMT and GA produced a more uneven complex than the one without MMT and CA (Figure 3.7.: f). These surface modifications indicate effective crosslinking and good interaction between MMT and the base polymer molecules [11, 12]. The roughness in surface morphology can enhance the adhesion of drug delivery systems to the intestinal wall, which is beneficial for localised treatment. The increased surface area enables more effective interaction with the mucosal layer, resulting in a prolonged retention time in the intestine and improved therapeutic efficacy [13].

3.1.4. Glucose uptake assay

Insulin resistance is a key characteristic of type 2 diabetes mellitus. The insulin signalling pathway is activated when insulin attaches to its specific receptor on cells that respond to insulin, triggering a cascade of signals that promote the movement of the GLUT4 glucose transporter from the cytoplasm to the cell surface, facilitating glucose entry into the cells [11]. It is well recognised that elevated circulating saturated free fatty acids, especially palmitate, disrupt insulin signalling and contribute to insulin resistance [12]. Given that skeletal muscle cells are responsible for over 70% of insulin-mediated glucose transport, we examined the impact of our LA-loaded PECs on averting palmitate-induced insulin resistance in skeletal muscle cells.

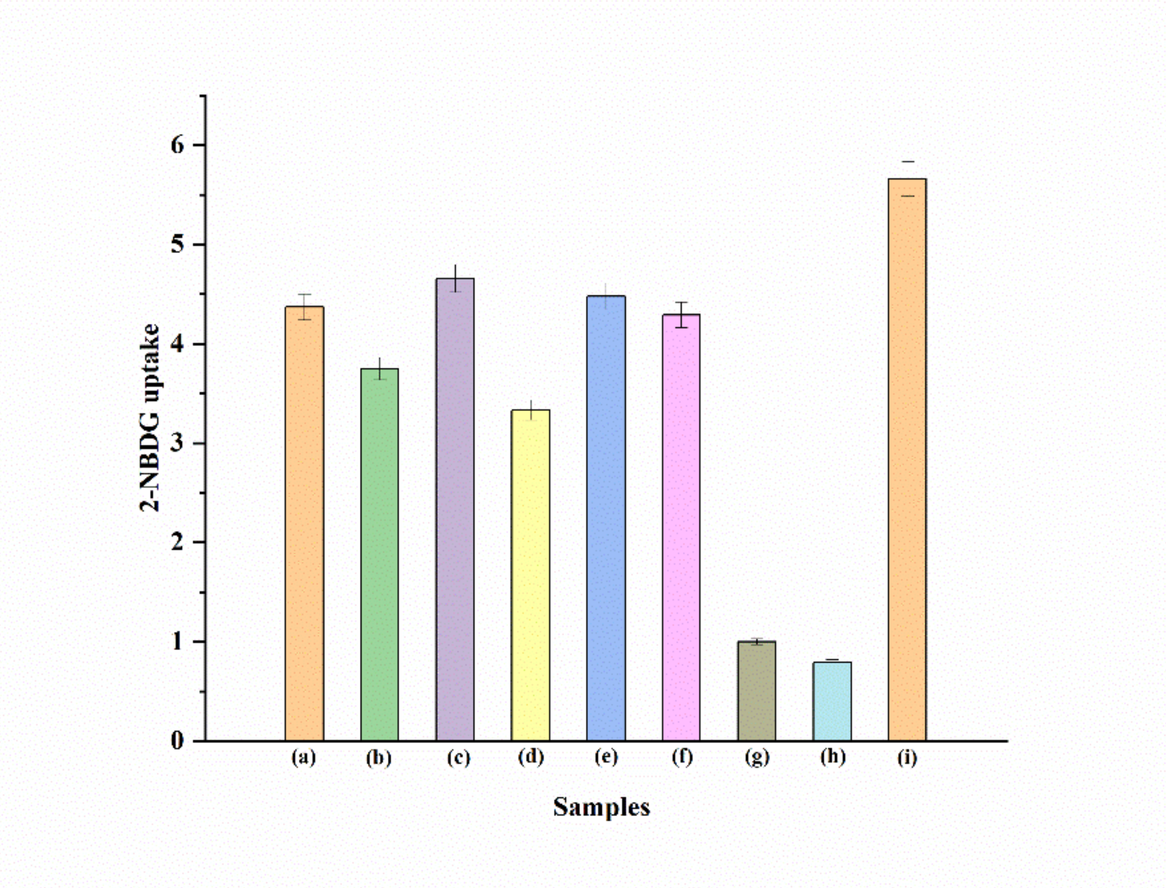

Figure. 3.8. Glucose uptake assay performed for (a) CA/GA2/M2, (b) CA/M3, (c) CA/M1, (d) CA/GA3, (e) CA/GA1, (f) CA, (g) Control, (h) Palmitate, (i) Insulin

The formulations significantly mitigated the impairment of insulin-stimulated 2-NBDG uptake in L6 myotubes caused by palmitate. The control group's glucose uptake was significantly lower than that of all treated groups, illustrating the basal glucose transport activity in the absence of stimulation. In contrast, the palmitic acid group served as a pathological control, showing decreased glucose uptake characteristic of lipid-induced insulin resistance. This reduction in glucose uptake is consistent with the dysregulated metabolic state observed in type 2 diabetes, where lipid accumulation in muscle tissues impairs insulin signalling pathways.

All of our samples significantly enhanced glucose uptake in the cells. The formulations could help lower blood glucose levels in circulation by promoting glucose uptake into peripheral cells. Samples containing 0.3% w/w MMT exhibited marginally higher glucose uptake compared to MMT-free CA. Glucose uptake was found to decrease with the increase in MMT concentration. The inclusion of MMT controlled the release of LA due to the presence of intricate silicate layers. A higher percentage of MMT incorporation hindered LA's release efficiently, reducing its glucose uptake effectiveness. Similarly, adding GA at a lower percentage didn’t significantly improve the glucose uptake. Still, a higher concentration of GA incorporation reduced glucose uptake due to the reduced availability of LA resulting from the compact structure caused by cross-linking. However, the combined addition of GA and MMT exhibited similar levels of glucose uptake. Consequently, these findings suggest the potential of developing lipoic acid-loaded systems as effective hypoglycaemic agents. CA/M1, CA/GA1, CA, and CA/GA2/M2 showed the best results. This comparatively better performance can be attributed to a combination of factors, including improved drug loading, enhanced drug release, and the impact of the formulations on the vitality and metabolic activities of the cells [13, 14]. These findings are consistent with previous studies that have demonstrated the efficacy of lipoic acid in improving insulin sensitivity and glucose uptake. For instance, Midaoui et al. reported that α-lipoic acid plays a role in preventing insulin resistance by enhancing glucose uptake in peripheral tissues [15]. Similarly, Lee et al. demonstrated that lipoic acid enhances glucose uptake by activating AMP-activated protein kinase (AMPK) in skeletal muscle cells, thereby improving insulin sensitivity [16].

3.1.5. Cell viability assay

The cell viability assays, conducted using the MTT method, demonstrated that all tested formulations exhibited excellent biocompatibility with no significant cytotoxicity observed across the tested concentrations.

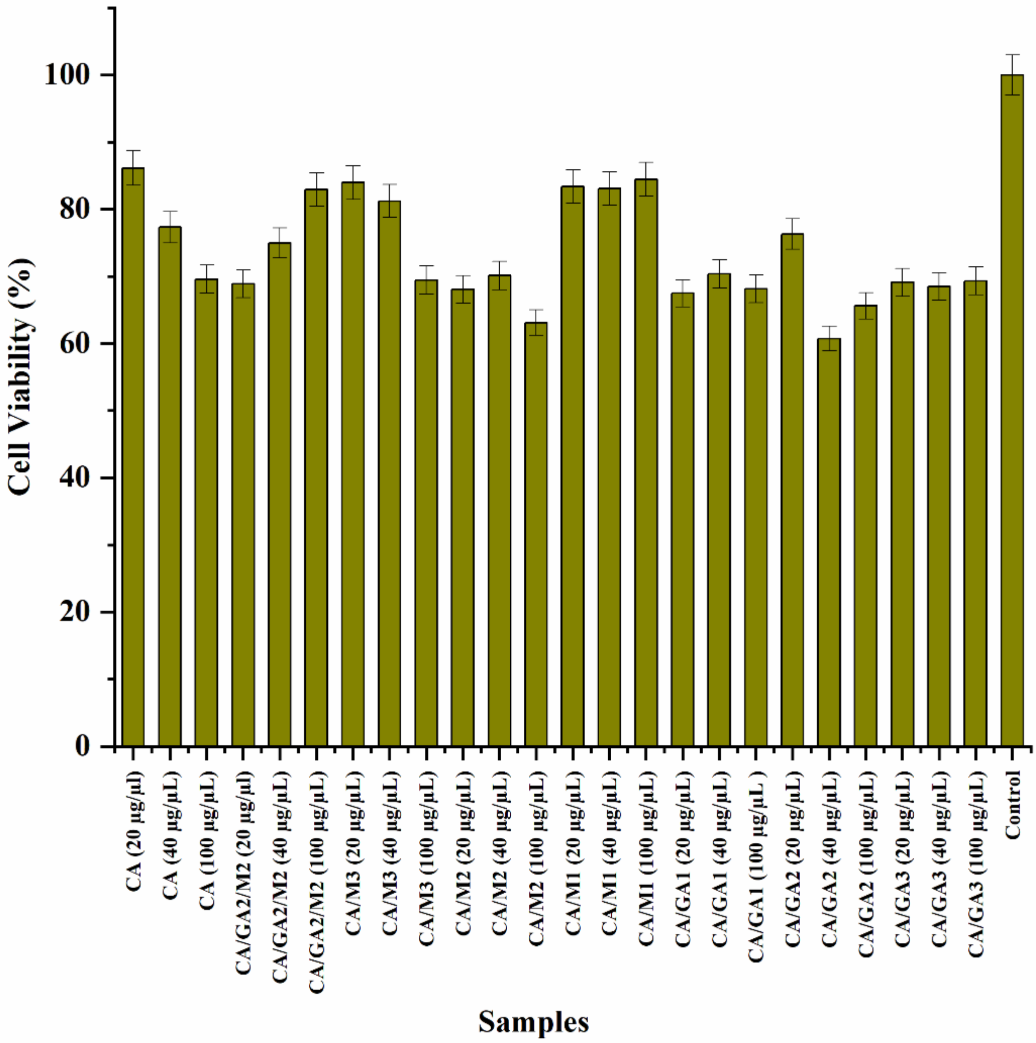

Figure 3.9. Cytotoxicity assay performed for the lipoic acid-loaded systems with varying concentrations of GA and MMT

Cell viability studies indicated a dose-dependent response in cell lines treated with higher concentrations of Montmorillonite (MMT), specifically in samples such as CA/M3. This response was attributed to the reduced release of lipoic acid (LA) from these formulations. Conversely, samples containing a lower percentage of MMT (CA/M1) displayed the highest cell viability and did not exhibit a dose-dependent response. The silicate layers within MMT played a crucial role in controlling the release of LA and influencing cell viability. Additionally, variations in the percentage of glutaraldehyde across the samples did not significantly impact cell viability, suggesting that differences in crosslinker concentration were not detrimental. The formulation containing both MMT and glutaraldehyde (CA/GA/M2) elicited a dose-dependent increase in cell viability in diabetic cell lines, likely due to the enhanced availability of LA. In contrast, formulations devoid of MMT or crosslinkers displayed slight cytotoxicity at higher doses, underscoring that cell viability depends on the availability of LA, which is regulated by the amount of crosslinker present.

Our findings are consistent with previous studies highlighting the biocompatibility of chitosan and alginate-based drug delivery systems. For instance, Prabaharan and Mano reported that chitosan-based particles are well-tolerated in cellular systems due to their biodegradability and non-toxic nature [17]. Similarly, studies by Oliveira et al. confirmed that biopolymer films crosslinked with GA, when used at controlled concentrations, exhibit good biocompatibility without inducing significant cytotoxic effects [18].

George and Shrivastav observed that excessive GA crosslinking reduced cell viability in alginate-based hydrogels, potentially due to the formation of rigid polymer networks that hinder cell proliferation [19]. In contrast, our formulations with higher GA concentrations did not show significant cytotoxic effects. This is likely due to the optimised balance between crosslinker concentration and the biopolymer matrix, which preserved the formulations’ overall structural flexibility and biocompatibility.

Moreover, our findings align with the research of Marapureddy and Thareja, who demonstrated that including nanofillers, such as MMT, can improve the mechanical strength of the delivery system without negatively impacting cell viability [20]. In our study, the incorporation of MMT at lower concentrations (e.g., CA/M1) improved cell viability, suggesting that moderate levels of MMT can enhance the mechanical properties of the formulations without compromising biocompatibility.

Overall, our study demonstrates that careful modulation of both GA and MMT concentrations can maintain or even enhance cell viability, reinforcing the potential of these formulations for future drug development. By optimising these parameters, we have successfully created a system that improves therapeutic efficacy and ensures cell safety, particularly in long-term treatments for chronic diseases such as type 2 diabetes.

3.2. GELATIN-HALLOYSITE NANOTUBE-CARRAGEENAN POLY-ELECTROLYTE COMPLEX FOR PH-RESPONSIVE DELIVERY OF LIPOIC ACID

3.2.1. Process yields, drug encapsulation efficiency, and drug loading efficiency

The process yield was calculated using the formula provided in section 2.2.7 (Chapter 2) and Table 3.2. presents the yield, encapsulation efficiency, and drug loading efficiency results for various Gelatin A/Carrageenan-based polymer systems developed for delivering lipoic acid (LA). These results highlight the effects of varying halloysite nanotube (HNT) and glutaraldehyde (GA) concentrations on the properties of the complexes.

HNT and GA concentration variations do not exhibit any specific trend in process yield (%). The irregular trend is possibly due to material loss during isolation, a phenomenon also observed in other crosslinked polymeric systems. When examining encapsulation and loading efficiencies, a notable trend emerged: as the HNT content increased, both encapsulation efficiency and drug loading efficiency improved. This enhancement can be attributed to the nanotubular structure and high aspect ratio of HNT, which provide additional surface area and facilitate more robust intermolecular interactions between the drug and the polymeric matrix [21]. Specifically, the abundant –OH groups on the HNT surface can form hydrogen bonds with functional groups of Gelatin A (–NH_2, –COOH) and carrageenan (–SO_4, –COOH), encouraging the polymer chains to adopt extended or more rigid conformations [22]. These structural modifications create a more organised and compact matrix environment that better retains the drug molecules, thus boosting encapsulation and loading efficiencies.

Table 3.2. Effect of GA and HNT on properties of Lipoic Acid loaded Gelatin-Carrageenan complex*

Sample Code[(a)]	**Gelatin % w/v (amount in g in 50 mL water)**	**Carrageenan % w/v (amount in g in 50 mL water)**	**Amount of crosslinker, % v/w (in µL)**	**Amount of HNT clay, % w/w w.r.t. GC (g in 50mL water)**	**Process Yield (%)**	**Encapsulation Efficiency (%)**	**Drug Loading Efficiency (%)**
GC	0.1 (0.05)	0.3 (0.15)	0	0	72.3 (±0.02)	80.3 (±0.02)	53.2 (±0.03)
GC/GA1	0.1 (0.05)	0.3 (0.15)	2.5 (5)	0	71.5 (±0.03)	79.5 (±0.04)	51.8 (±0.04)
GC/GA2	0.1 (0.05)	0.3 (0.15)	5.0 (10)	0	77.1 (±0.02)	76.8 (±0.02)	49.3 (±0.02)
GC/GA3	0.1 (0.05)	0.3 (0.15)	7.5 (15)	0	69.8 (±0.01)	75.1 (±0.05)	41.9 (±0.05)
GC/H1	0.1 (0.05)	0.3 (0.15)	0	0.3 (0.06)	80.8 (±0.03)	80.8 (±0.04)	56.4 (±0.04)
GC/H2	0.1 (0.05)	0.3 (0.15)	0	1.2 (0.24)	79.5 (±0.04)	81.2 (±0.05)	58.2 (±0.01)
GC/H3	0.1 (0.05)	0.3 (0.15)	0	4.8 (0.96)	82.1 (±0.01)	83.4 (±0.01)	59.9 (±0.04)
GC/GA2/H2	0.1 (0.05)	0.3 (0.15)	5.0 (10)	1.2 (0.24)	80.63 (±0.04)	79.2 (±0.03)	55.3 (±0.01)

Lipoic Acid = 0.01g, Tween 80 = 0.015 mL.

(a) In the sample code, Gelatin-Carrageenan PEC, glutaraldehyde, and HNT are represented by "GC," "GA," and "H," respectively.

*Each value and the standard deviation in parentheses represent the average of five readings.

The interaction of HNT with the polymer network can also lead to the formation of a porous structure during dehydration, which includes small channels extending from the interior to the outer surface of the complex [23]. While such porosity is sometimes associated with enhanced drug release, careful optimisation of HNT content and crosslinking density can counterbalance premature diffusion, ultimately supporting higher encapsulation and loading [24]. Further, incorporating GA as a crosslinker may reduce polymer chain mobility, encouraging network rigidity and potentially increasing porosity. At elevated GA concentrations, these changes could allow the drug to migrate through pores and channels from the complex interior to the surrounding medium, thereby diminishing encapsulation and loading efficiencies [25]. However, the positive effects of HNT incorporation can mitigate these losses by providing a more structured and interactive environment for the drug.

Overall, increasing HNT concentration fosters a more favourable microenvironment for drug retention within Gelatin A/Carrageenan complexes, enhancing encapsulation and loading efficiencies, even in the presence of increased cross-linking. This improvement aligns with observations in other biopolymer-HNT composites, where the inclusion of nanotubes enhances drug loading capacity, demonstrating the versatile applicability of HNT in drug delivery systems.

3.2.2. *In Vitro* Release Studies

The *in vitro* release profile of lipoic acid (LA) from a glutaraldehyde-crosslinked gelatin-halloysite-carrageenan polyelectrolyte complex was investigated over a 1- to 50-hour period at two pH levels, 1.2 and 7.4. The cumulative release percentage of LA was found to be pH-dependent, with higher release rates observed in the alkaline medium (pH 7.4) compared to the acidic medium (pH 1.2).

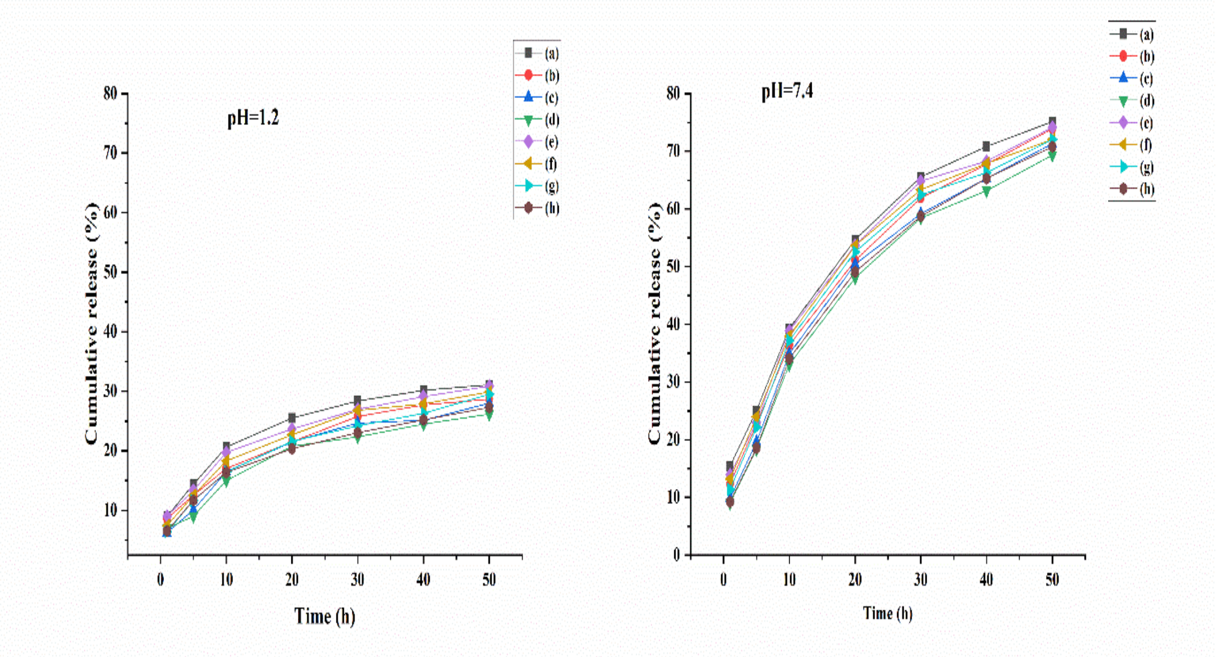

Figure 3.10. The cumulative drug release profile for (a) GC, (b) GC/M1, (c) GC/M2, (d) GC/M3, (e) GC/GA1, (f) GC/GA2, (g) GC/GA3, (h)GC/GA2/M2

At pH 1.2, gelatin molecules become protonated, enhancing their electrostatic interactions with the negatively charged sulfate groups of carrageenan. This results in the formation of a more compact and denser polyelectrolyte complex, which reduces the matrix's swelling capacity and restricts the diffusion of LA. Consequently, the rate of LA release decreases in an acidic environment due to the tighter network structure, which limits solvent penetration.

In contrast, at pH 7.4, deprotonation of gelatin reduces its interaction with carrageenan, leading to a looser polymer network. This increases the swelling of the complex, allowing more solvent access to the encapsulated LA. The breakdown of hydrogen bonds between the polymer matrix and LA at higher pH levels promotes drug release, resulting in a higher cumulative release percentage. The enhanced swelling under alkaline conditions improves the diffusion pathways for LA, thereby accelerating its release from the complex.

The data also demonstrated that the cumulative release of LA decreased with increasing concentrations of halloysite nanotubes (HNTs) and glutaraldehyde (GA). Incorporating HNTs introduces silicate layers that act as physical barriers, impeding solvent molecules from penetrating the complex. A higher HNT content intensifies this barrier effect, restricting solvent access to the encapsulated LA and thereby decreasing its release rate.

Similarly, increasing the GA concentration enhances the crosslinking density within the polyelectrolyte complex. A higher degree of crosslinking results in a more rigid and less permeable network structure, further limiting solvent diffusion. This denser matrix effectively traps LA, leading to a decrease in its cumulative release over time.

These findings suggest that by modulating the pH and adjusting the concentrations of HNTs and GA, it is possible to control the release profile of LA from the gelatin-halloysite-carrageenan polyelectrolyte complex. The ability to tailor the drug release behaviour makes this system a promising candidate for targeted and controlled drug delivery applications.

3.2.3. Characterisation

3.2.3.1. Fourier transform infrared spectroscopy

Gelatin-A typically displays broad absorptions for N–H and O–H stretching between 3100 and 3400 cm^{-1}, indicative of both peptide backbone amides and bound water. Its amide I band (~1650 cm^{-1}) corresponds primarily to C=O stretching of peptide bonds, while the amide II band (~1540 cm^{-1}) arises from N–H bending and C–N stretching [26]. Carrageenan, a sulfated polysaccharide, presents a broad O–H stretching region around 3200–3400 cm^{-1}, reflecting its extensive hydrogen-bonding network. Its sulfate ester groups yield characteristic S=O stretching vibrations typically observed near 1220–1250 cm^{-1}. The carrageenan backbone's glycosidic C–O–C stretches appear in the 1000–1150 cm^{-1} range [27]. The formation of a polyelectrolyte complex through electrostatic interactions between the positively charged regions of gelatin and the negatively charged sulfate groups of carrageenan resulted in subtle shifts in these bands. Such shifts and changes in intensity ratios in the amide and sulfate regions confirm the establishment of intermolecular interactions within the hybrid matrix.

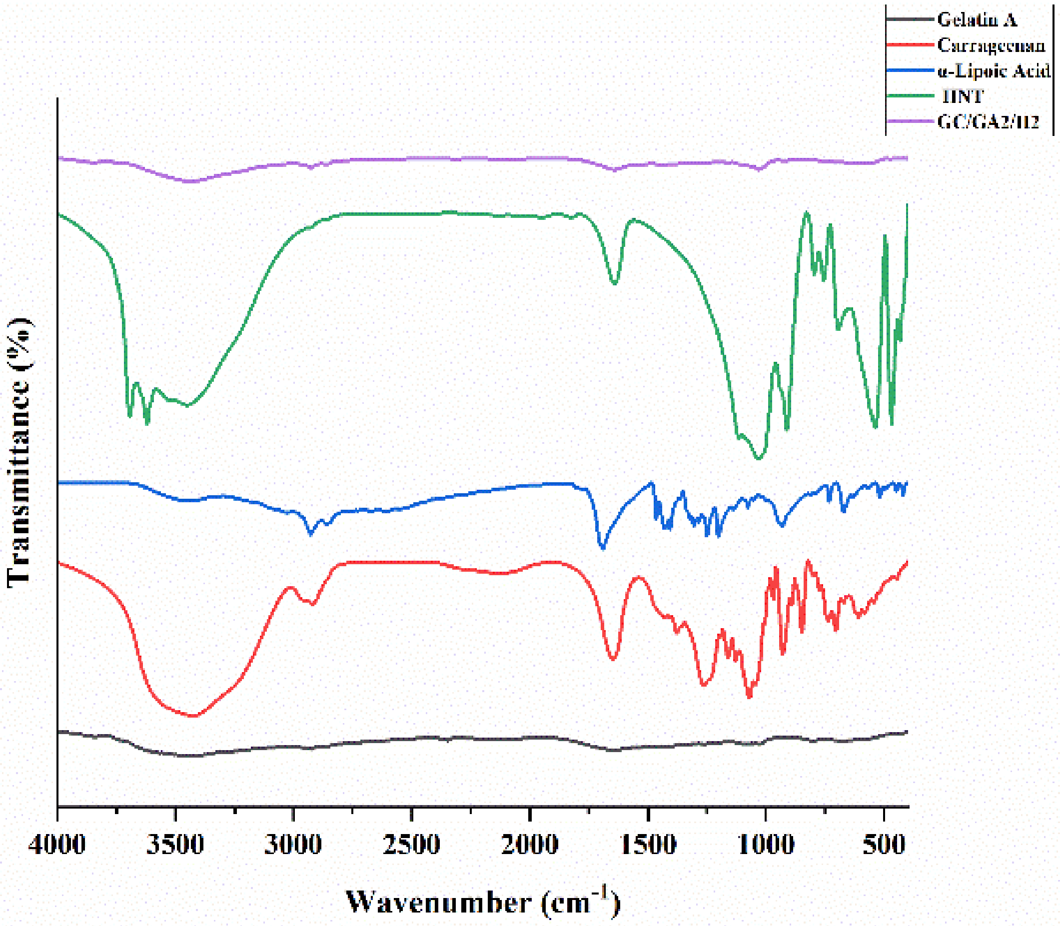

Figure 3.11. FTIR spectra of the product and the raw materials.

The use of glutaraldehyde as a crosslinker typically induces minor shifts in the amide I and II regions due to the formation of covalent bonds between the aldehyde groups and the free amino residues in gelatin. This crosslinking can slightly increase the rigidity of the biopolymer network and may lead to small wavenumber shifts or intensity changes in the amide I band [28]. The addition of halloysite nanotubes introduces characteristic signals of aluminosilicate structures. Si–O–Si and Al–O–Si stretching vibrations generally occur between 1000 and 1100 cm^{-1} [29]. The presence of these absorptions in the composite's spectrum confirmed the successful incorporation of HNT. The interaction between the biopolymeric matrix and HNT surfaces broadened or slightly shifted polymeric bands, reflecting hydrogen bonding or electrostatic interactions at the organic-inorganic interface.

Encapsulated lipoic acid (LA), containing a carboxylic acid moiety, contributes distinct C=O stretching bands in the approximately 1700–1720 cm^{-1} region [30]. The O–H stretch of the carboxyl group appears as a broad absorption, overlapping with the biopolymers' broad O–H/N–H region. Although the disulfide bond of LA is weakly IR-active, its presence can nonetheless influence the local chemical environment. Interactions between LA and the gelatin–carrageenan–HNT matrix led to subtle spectral changes, particularly in regions associated with hydrogen bonding and carbonyl absorptions.

The IR spectrum of GC/GA2/H2 reflects the characteristic functional groups of each component and the interactions that arise from their combination. The encapsulation of lipoic acid within this matrix introduces additional features, most notably related to the presence of its carboxylic acid groups.

The IR spectral data validate the formation of a structurally coherent, crosslinked gelatin–carrageenan polyelectrolyte complex incorporating halloysite nanotubes and encapsulating lipoic acid. Characteristic amide (gelatin), sulfate and glycosidic (carrageenan), silicate (HNT), and carboxylic (LA) absorptions are evident. Shifts in key bands, notably in the amide and sulfate regions, and the appearance of distinct carbonyl peaks from LA's carboxylic groups confirm the successful integration of each component. These spectral signatures collectively demonstrate the establishment of intermolecular interactions, improved matrix rigidity through crosslinking, and effective encapsulation of lipoic acid.

3.2.3.2. X-ray diffraction study

Lipoic acid (LA) exhibits distinct sharp peaks at 2θ = 23° and 2θ = 19°, which indicate its crystalline nature. The diffractogram of the GC system showed a distinct broad peak at 2θ = 42°. The characteristic peaks for lipoic acid disappeared in the diffractogram of the drug-loaded complex. This suggests the formation of an amorphous region, likely due to the suppression of the drug's crystallisation within the confinement of the polymer matrix [8, 9]. This also indicates the molecular-level dispersion of LA within the complex and the amorphous or disordered crystalline nature of LA in the polymer matrix. The transition to an amorphous state (as suggested by the disappearance of these peaks in Figure 3.12 for drug-loaded formulations) can significantly enhance the drug's solubility and bioavailability.

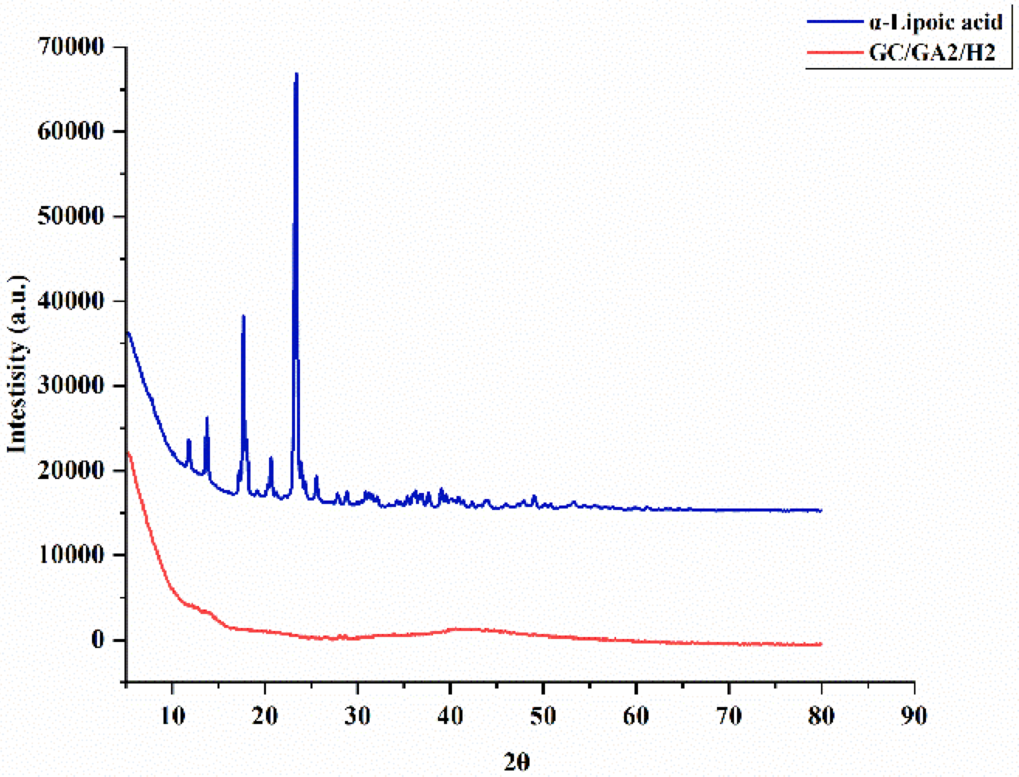

Figure 3.12. XRD Pattern of Lipoic Acid and GC/GA2/H2

3.2.3.3. Field-Emission Scanning Electron Microscopy (FESEM) Analysis

FESEM was employed to investigate the surface morphology of the Gelatin-Halloysite Nanotube (HNT)-Carrageenan polyelectrolyte complexes loaded with lipoic acid.

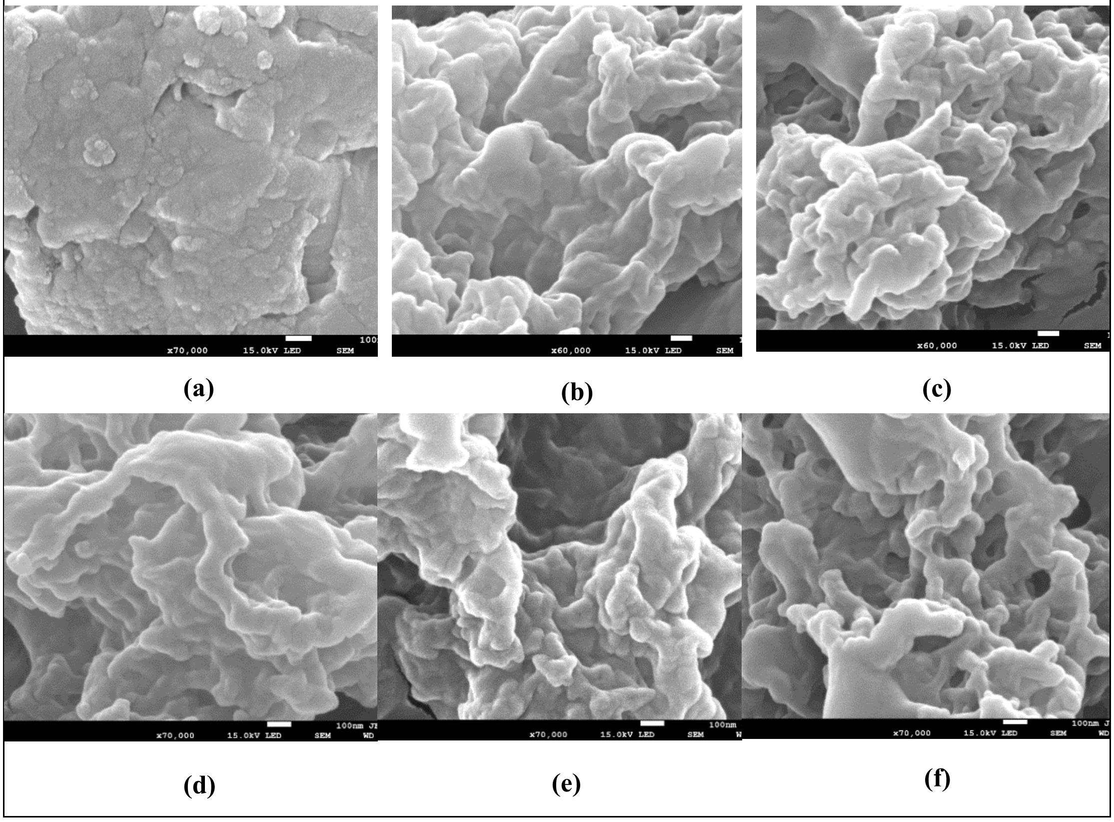

(a) (b) (c)

(d) (e) (f)

Figure 3.13. FESEM images of (a) GC, (b) GC/GA1, (c) GC/GA3, (d) GC/M1, (e) GC/M3, (f)GC/GA2/M2

The pristine gelatin matrix exhibited a relatively smooth and continuous surface (Figure 3.13.a). Subtle surface irregularities emerged after incorporating HNTs at lower concentrations (Figure 3.13.b), suggesting initial HNT dispersion within the polyelectrolyte network. These nanotubes, which inherently possess elongated tubular structures, remained partially embedded within the gelatin-carrageenan matrix, producing mild undulations without substantial agglomeration. As the HNT concentration increased (Figure 3.13.c), the surface became more textured, indicative of enhanced nanotube aggregation and stronger polymer-nanotube interactions. This texturisation has been attributed to hydrogen bonding and electrostatic attractions between the negatively charged carrageenan, the positively charged gelatin segments, and the aluminosilicate framework of HNT, resulting in a denser polymer network [31]. Furthermore, adding crosslinking agents at higher concentrations (Figure 3.13.e) led to more pronounced matrix densification, manifested by tighter structural features and increased roughness on the complex surface. These modifications suggest efficient crosslinking between the amine groups of gelatin and the sulfate groups of carrageenan, further stabilised by interactions with HNT.

Incorporating both HNT and crosslinkers thus yielded polyelectrolyte complexes with enhanced textural complexity compared to their counterparts without HNT. Such roughened surfaces are advantageous for site-specific oral drug delivery as they can promote stronger adhesion to the intestinal mucosa, prolonging local residence time and improving therapeutic effectiveness. These nanotubes may also contribute to the pH-responsive release of lipoic acid, as the interpolymeric crosslinks can undergo conformational changes in varying gastrointestinal pH conditions, optimising drug release profiles for improved bioavailability [32].

3.2.4. 2-NBDG uptake assay

The 2-NBDG uptake assay was employed to evaluate the effects of lipoic acid-loaded gelatin–carrageenan nanoparticles, which were prepared by varying the concentration of glutaraldehyde (GA) crosslinking agent and Halloysite nanotubes (HNT) on glucose uptake in L6 myotubes. The assay results indicate that crosslinking density and HNT concentration have a significant influence on cellular metabolic activity.

As expected, untreated control cells presented baseline 2-NBDG uptake, whereas insulin-treated cells presented a marked increase in glucose uptake (Figure 3.14., samples a and b). This positive control confirmed the assay’s sensitivity in detecting increased glucose uptake under conditions of enhanced insulin sensitivity. In contrast, cotreatment with insulin and palmitate significantly reduced glucose uptake (Figure 3.14., sample c), consistent with the literature on fatty acid-induced insulin resistance and impaired insulin signalling, thereby reducing glucose uptake in muscle cells [33, 34]. This condition serves as a model of metabolic impairment, providing a comparative basis for assessing the efficacy of nanoparticles in potentially restoring or enhancing glucose uptake.

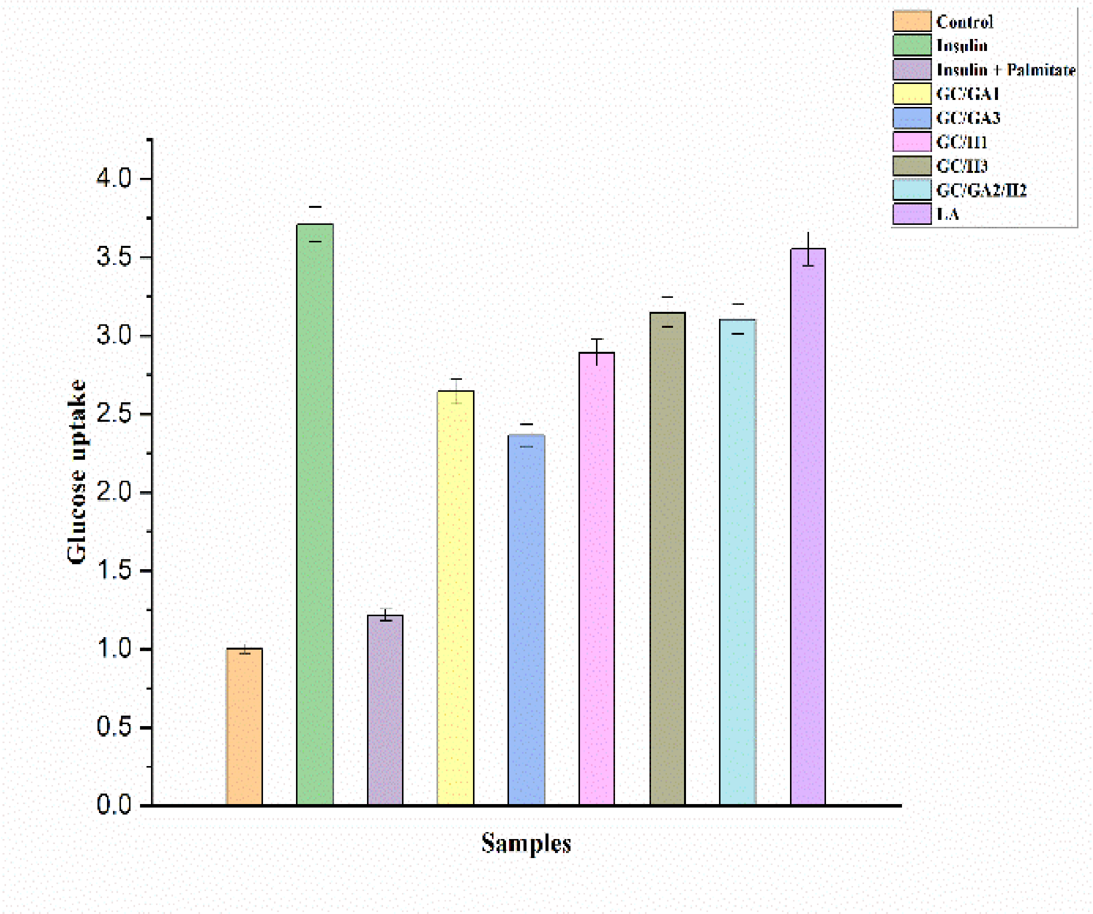

Figure 3.14. Glucose uptake assay results for the samples

The lipoic acid-loaded formulations with higher GA concentrations (Figure 3.14, samples d: GC/GA3 and e: GC/GA2) exhibited a notable decrease in 2-NBDG uptake compared to insulin-treated cells. This trend aligns with previous studies indicating that increased crosslinking density can result in reduced nanoparticle flexibility and diminished cellular interaction, thereby hindering metabolic function [35]. Reduced flexibility from increased crosslinking density likely limits the nanoparticles' cellular uptake, attenuating lipoic acid’s bioavailability and potential effects on glucose metabolism. In contrast, nanoparticles with a lower crosslinking density (Figure 3.14., sample f: GC/GA1) maintained relatively high glucose uptake. These findings suggest moderate crosslinking levels may support structural stability without significantly compromising cellular uptake. A balanced degree of crosslinking appears to be critical for optimal interactions with cellular membranes, enhancing the metabolic effects of curcumin.

Variations in the HNT concentration within the nanoparticles also affected the uptake of 2-NBDG. The increase in HNT concentration in the PECs corresponded to an increase in glucose uptake, suggesting that HNT at these levels may positively influence cellular bioactivity. The combined formulation with moderate GA crosslinking and HNT (Figure 3.14., sample h: GC/GA2/H2) also demonstrated good glucose uptake.

Lipoic acid alone (Figure 3.14, sample l) increased glucose uptake. Curcumin modulates inflammatory pathways and antioxidant responses, alleviating cellular stress and enhancing glucose uptake. This result aligns with the hypothesis that lipoic acid can positively impact glucose metabolism even when delivered without additional modifications, highlighting its therapeutic potential in metabolic disorders [36].

Overall, the 2-NBDG uptake results suggest that lipoic acid-loaded gelatin–carrageenan nanoparticles, particularly those with lower GA crosslinking and higher HNT concentrations, enhance glucose uptake in L6 myotubes. The optimal balance of GA and HNT is essential to maintain biocompatibility and maximise glucose uptake.

3.2.5. Cell viability assay

Cell viability was evaluated using an MTT assay in cell lines exposed to various concentrations (20 µg/µL, 40 µg/µL, 100 µg/µL) of lipoic acid-loaded gelatin-carrageenan polyelectrolyte complexes (PECs), which were modified by differing concentrations of glutaraldehyde (GA) and halloysite nanotubes (HNT). Untreated cells were employed as controls, establishing a baseline viability of 100%, which is essential for assessing the relative impact of each formulation.

Cells treated with the base gelatin-carrageenan formulation (GC) exhibited near-baseline viability at 20 µg/µL. However, increasing the concentration resulted in a modest decrease in viability, suggesting that the polymer concentration may induce cellular stress at higher levels. A progressive decline in cell viability was observed with increasing glutaraldehyde concentrations (from GC/GA1 to GC/GA3), implicating the cytotoxic potential of glutaraldehyde. This decrease is likely due to increased matrix rigidity and chemical reactivity, which could disrupt cellular functions [18, 19]. In contrast, introducing HNTs (from GC/H1 to GC/H3) generally improved cell viability, with the highest HNT concentration showing viability comparable to the untreated control at lower dosages. This enhancement may be attributed to the HNTs' ability to modulate the matrix properties, thereby reducing cytotoxicity. GC/GA2/H2 formulation maintained higher viability than high GA samples. It was comparable to high HNT samples, suggesting that a moderate level of cross-linking coupled with HNT reinforcement could synergistically improve the biocompatibility of the PECs [37, 38]. These findings highlight the critical need to balance the components within biopolymeric drug delivery systems to optimise biocompatibility and therapeutic efficacy.

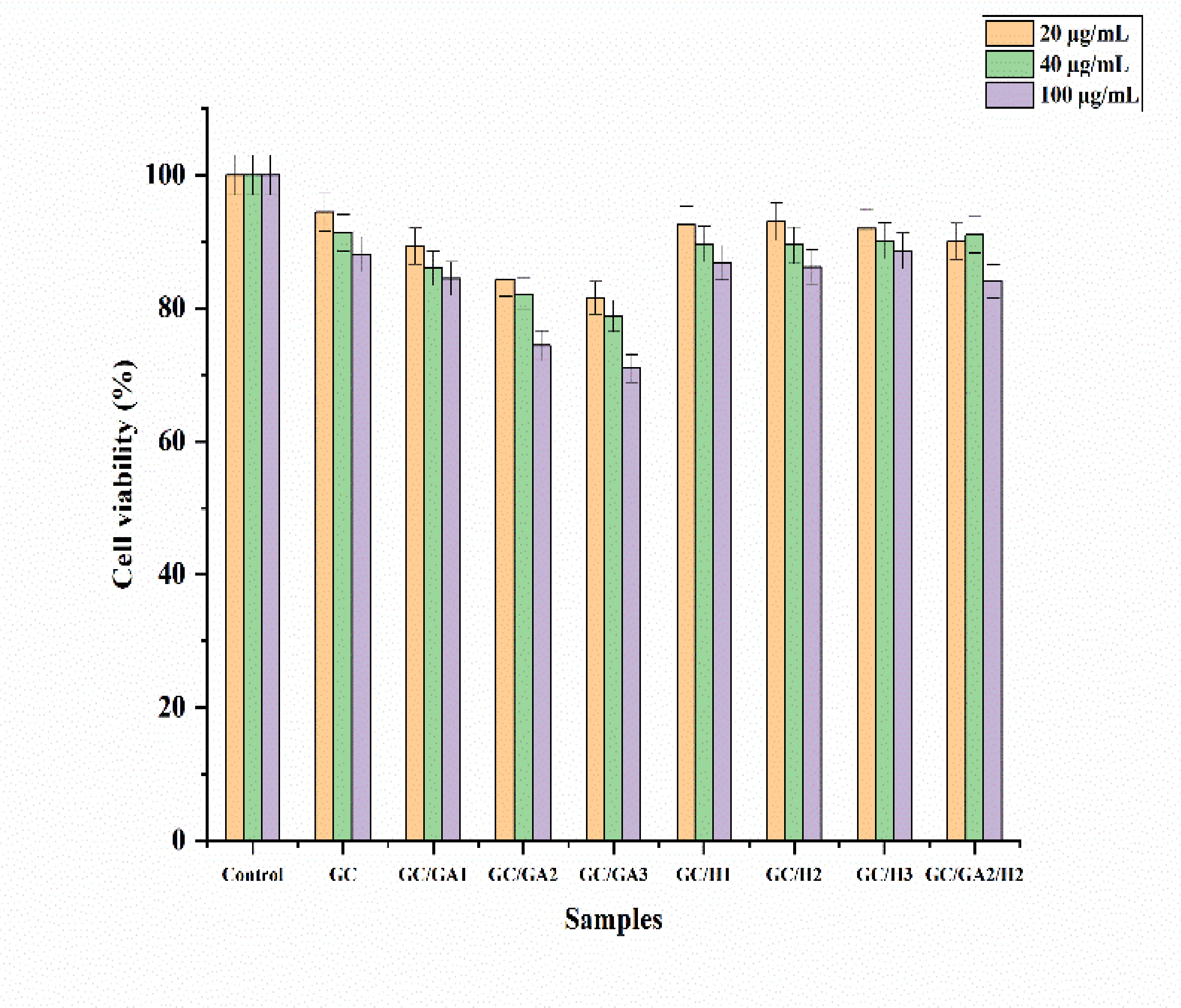

Figure 3.15. Cytotoxicity assay performed for the lipoic acid-loaded GC systems with varying concentrations of GA and HNT

3.3. MAGNESIUM OXIDE-DOPED CHITOSAN-CARRAGEENAN COMPLEX FOR CONTROLLED ORAL DELIVERY OF CURCUMIN

3.3.1. Process yield, drug loading and drug encapsulation efficiency

The process yield of the nanoparticle formulations was determined via the equation provided in section 2.2.7 (Chapter 2). Table 3.3. summarises the process yields (%) encapsulation and drug loading efficiencies (%) for various polymer systems developed for the delivery of curcumin, along with the impact of varying MgO and glutaraldehyde (GA) concentrations on the characteristics of chitosan (Ch)/carrageenan (Car) nanoparticles.

Table 3.3. Effects of GA and MgO on the Properties of Curcumin-loaded Chitosan-Carrageenan Nanoparticles

Sample Code	**Chitosan % w/v (amount in g in 50 mL water)**	**Carrageenan % w/v (amount in g in 50 mL water)**	**Amount of crosslinker, % v/w (in µL)**	**Amount of MgO nanoparticles, % w/w w.r.t. CC (g in 50 mL water)**	**Process Yield (%)**	**Encapsulation Efficiency (%)**	**Drug Loading Efficiency (%)**
CC	0.35 (17.5)	0.35 (17.5)	0	0	72.1 (±0.02)	67.8 (±0.03)	51.6 (±0.02)
CC/GA1	0.35 (17.5)	0.35 (17.5)	2.5 (5)	0	70.2 (±0.03)	64.9 (±0.02)	48.3 (±0.03)
CC/GA2	0.35 (17.5)	0.35 (17.5)	5 (10)	0	68.4 (±0.02)	61.2 (±0.04)	45.1 (±0.02)
CC/GA3	0.35 (17.5)	0.35 (17.5)	7.5 (15)	0	65.9 (±0.03)	58.5 (±0.03)	41.7 (±0.05)
CC/MO1	0.35 (17.5)	0.35 (17.5)	0	0.5 (0.175)	73.4 (±0.02)	65.6 (±0.03)	43.2 (±0.04)
CC/MO2	0.35 (17.5)	0.35 (17.5)	0	1.0 (0.35)	74.8 (±0.02)	62.3 (±0.04)	40.9 (±0.03)
CC/MO3	0.35 (17.5)	0.35 (17.5)	0	1.5 (0.45)	74.3 (±0.04)	61.9 (±0.01)	40.1 (±002)
CC/GA2/MO2	0.35 (17.5)	0.35 (17.5)	5 (10)	1.0 (0.35)	69.3 (±0.02)	59.1 (±0.03)	37.8 (±0.04)

Curcumin = 0.05 g, Tween 80 = 0.015 mL.

(a) In the sample code, chitosan-carrageenan (PEC), glutaraldehyde, and MgO nanoparticles are represented by “CC,” “GA,” and “MO,”, respectively.

*Each value and the standard deviation in parentheses represent the average of five readings.

The encapsulation efficiency of nanoparticles devoid of MgO was significantly greater than that of those containing MgO. A noticeable decline in encapsulation efficiency was observed with increasing MgO content in the nanoparticles. The inclusion of MgO reduces the space for drug entrapment, contributing to the observed decrease in encapsulation and loading efficiencies. Similarly, an increase in the GA concentration was found to reduce the encapsulation efficiency. As a crosslinking agent, GA restricts the free movement of polymer chains, thereby promoting the formation of a porous structure. This structure provided channels through which curcumin could migrate from the nanoparticle core to the preparation medium. Moreover, the interaction between GA and the polymer network resulted in a more compact and rigid structure, reducing the free volume for entrapment of curcumin within the polymer matrix. As a consequence, both the encapsulation and drug loading efficiencies are compromised. Notably, variations in the concentrations of GA and MgO did not significantly impact the overall process yield

3.3.2. *In vitro* drug release study

The *in vitro* release analysis of curcumin from MgO-doped chitosan-carrageenan nanoparticles was conducted under two distinct pH conditions, 1.2 and 7.4, for 1 to 50 h. The cumulative release profiles exhibited a clear pH dependency, with a significantly greater release rate in the alkaline medium (pH 7.4) than in the acidic medium (pH 1.2).

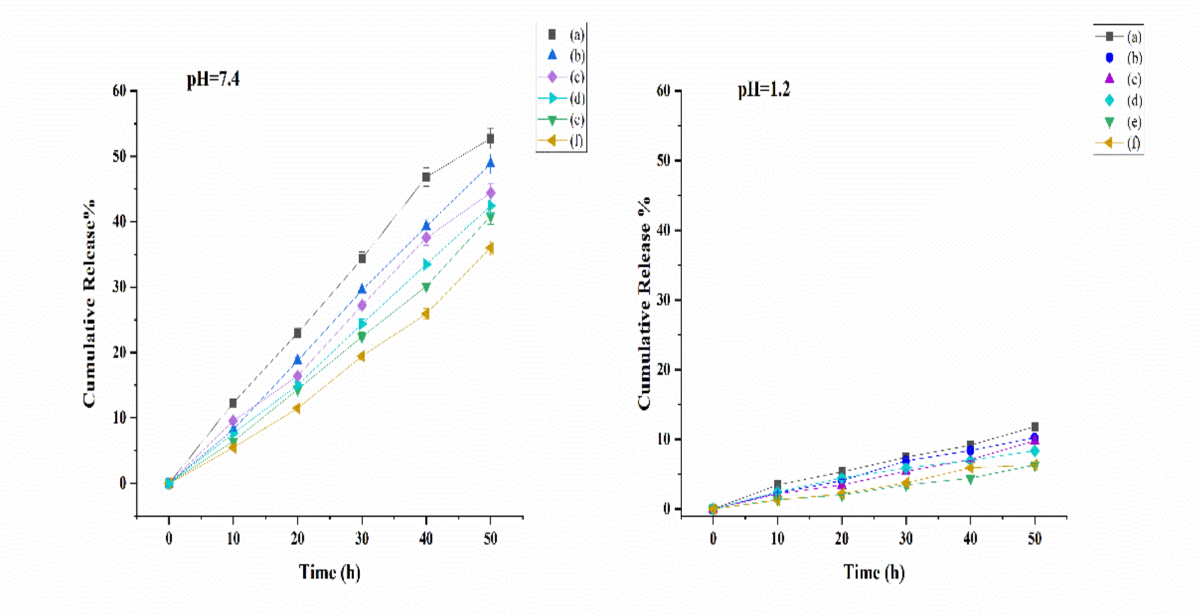

Figure 3.16. The cumulative drug release profile for (a) CC, (b) CC/MO1, (c) CC/MO3, (d) CC/GA1, (e) CC/GA3, and (f) CC/GA2/MO2

At pH 1.2, curcumin release was limited because a dense network structure formed between carrageenan and chitosan. This polyelectrolyte complex maintained structural integrity under acidic conditions, where strong electrostatic interactions between the anionic groups of carrageenan and the cationic groups of chitosan facilitated a compact matrix [3]. Additionally, the presence of glutaraldehyde (GA) as a crosslinking agent reinforced this network, restricting the mobility of curcumin within the nanoparticles and reducing its release [39]. Notably, MgO doping helped reduce burst release at this stage by contributing to the stability of the compact matrix, ensuring controlled, rather than rapid, release [40]. As the concentration of MgO increases, the release rate decreases, likely due to reduced swelling of the nanoparticles [41].

In contrast, at a pH of 7.4, the release of curcumin significantly increased. The alkaline conditions diminished the polymer matrix's hydrogen bonding and electrostatic interactions, leading to a more relaxed structural configuration [3]. The relaxation of the nanoparticles facilitated increased swelling and enhanced solvent penetration, promoting curcumin diffusion. The incorporation of MgO played a critical role in modulating the release profile under these conditions by increasing the porosity of the matrix. Moreover, the partial dissolution of MgO in an alkaline medium increased the local ionic strength, disrupting the interactions between the polymer and the drug and thereby accelerating the release of curcumin from the matrix. Consequently, MgO doping improved the release profile and mitigated the initial burst release, contributing to a more sustained release [40].

The extent of glutaraldehyde (GA) crosslinking significantly impacted the release kinetics. Elevated GA concentrations resulted in a more rigid matrix that limited curcumin release, whereas lower GA concentrations facilitated increased porosity and matrix swelling, especially under alkaline conditions [39]. This observation underscores the significant impact of crosslinking density on the modulation of curcumin release behaviour from the biopolymeric matrix, thereby facilitating a more pronounced release of curcumin.

3.3.3. Characterisation

3.3.3.1. Fourier transform infrared spectroscopy

Fourier transform infrared (FTIR) spectroscopy investigated the chemical interactions between chitosan, carrageenan, curcumin, and the drug formulation. The spectra of the individual components and the formulation were recorded, and the characteristic absorption bands were analysed to identify any potential chemical interactions or structural changes due to the formulation.

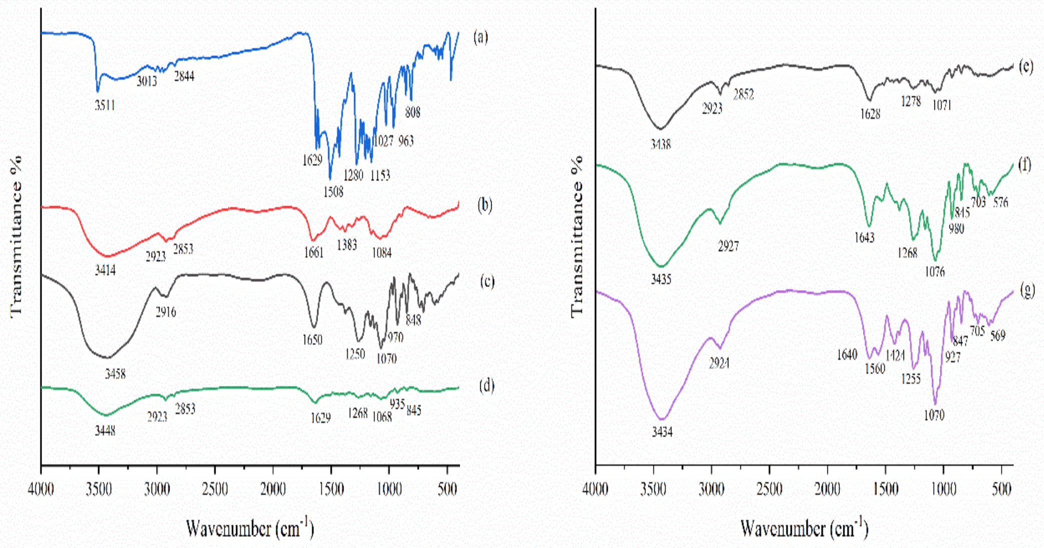

Figure 3.17. FTIR spectra of (a) Curcumin, (b) Carrageenan, (c) Chitosan, (d) CC complex, (e) CC/GA3, (f) CC/MO3, (g) CC/GA2/MO2

The FTIR spectrum of chitosan (curve (c), Figure 3.17.) exhibited a broad absorption band at approximately 3458 cm^{-1}, attributed to the overlap of O–H and N–H stretching vibrations, indicating the presence of hydroxyl and amino groups in the polysaccharide backbone. A prominent peak at 1650 cm^{-1} was observed, corresponding to the C=O stretching of the amide I band, whereas the peak at 1250 cm^{-1} was associated with N–H bending (amide II). Peaks in the 1070 cm^{-1} - 848 cm-1 range were assigned to C–O stretching vibrations, characteristic of the glycosidic bonds in chitosan [42].

The spectrum of carrageenan (curve (b), Figure 3.17) exhibited typical sulfate group absorption bands. Bands corresponding to the asymmetric and symmetric stretching vibrations of the S=O group were observed at 1380 cm^{-1}. The broad peak at approximately 3414 cm^{-1} was attributed to O–H stretching, whereas the peak near 1084 cm^{-1} was associated with C–O–C stretching, reflecting the glycosidic linkages within the carrageenan structure [43].

Curcumin (curve (a), Figure 3.17.), as expected, displayed a prominent peak at 1629 cm^{-1}, corresponding to the C=O stretching vibration, and characteristic peaks at approximately 1508 cm^{-1} due to the C=C stretching of the aromatic ring. The sharp peak at 1280 cm^{-1} is attributed to phenolic C=O stretching. The broad absorption band at approximately 3511 cm^{-1} was due to O–H stretching, indicating the presence of phenolic hydroxyl groups [44].

The formulation's FTIR spectrum of the curcumin-loaded MgO-doped chitosan–carrageenan (curve (d), Figure 3.17.) revealed notable changes in the absorption bands, indicating interactions between the biopolymers and curcumin. The broadening of the peak around the 3448 cm^{-1} region indicates strong hydrogen bonding within the matrix. A shift in the amide I band of chitosan from 1650 cm^{-1} to lower wavenumbers suggests the formation of hydrogen bonds between chitosan and carrageenan. Furthermore, compared with those of pure carrageenan, the intensities of the sulfate bands at 1220 cm^{-1} and 840 cm^{-1} were lower, indicating that the sulfate groups are involved in interactions with chitosan and curcumin in the formulation. The reduced intensity in the amine and sulfate regions (1650–1550 cm^{-1} and 1250–800 cm^{-1}) confirms the integration of the polymers. The shifts in the C=O stretching band and the stabilisation of the glycosidic peaks confirmed the successful incorporation of curcumin within the chitosan–carrageenan network. The spectrum of CC/GA3 (curve (e), Figure 3.17.) showed a broad O-H stretching peak at 3438 cm^{-1}, characteristic of the hydroxyl groups in the system. The prominent peak at 1628 cm^{-1} corresponds to C=O stretching vibrations, confirming that glutaraldehyde facilitated crosslinking. The additional peaks at 1278 cm^{-1} and 1071 cm^{-1} are attributed to S=O stretching from carrageenan and C-O-C stretching from glycosidic linkages, respectively. The spectrum of CC/MO3 (curve (f), Figure 3.17.) shows the presence of intense peaks at 703 cm^{-1} and 576 cm^{-1}, which are characteristic of MgO metal-oxygen (Mg–O) interactions. The spectrum of CC/GA2/MO2 (curve (g), Figure 3.17.) displayed features indicative of both glutaraldehyde and MgO contributions. A broad O-H stretching peak at 3434 cm^{-1} and a strong C=O stretching peak at 1640 cm^{-1} confirmed crosslinking by glutaraldehyde. A peak at 1560 cm^{-1} attributed to N–H bending also highlighted the interactions between chitosan and glutaraldehyde. Additionally, the spectrum showed metal–oxygen vibrations at 705 cm^{-1} and 569 cm^{-1}, confirming the presence of MgO.

3.3.3.2. X-ray diffraction study

The crystallinity and phase composition of chitosan, carrageenan, MgO, curcumin, and the MgO-doped chitosan–carrageenan nanoparticles were analysed via powder X-ray diffraction (XRD). The XRD patterns provided insights into the structural properties and confirmed the successful formation of biopolymeric nanoparticles for curcumin delivery.

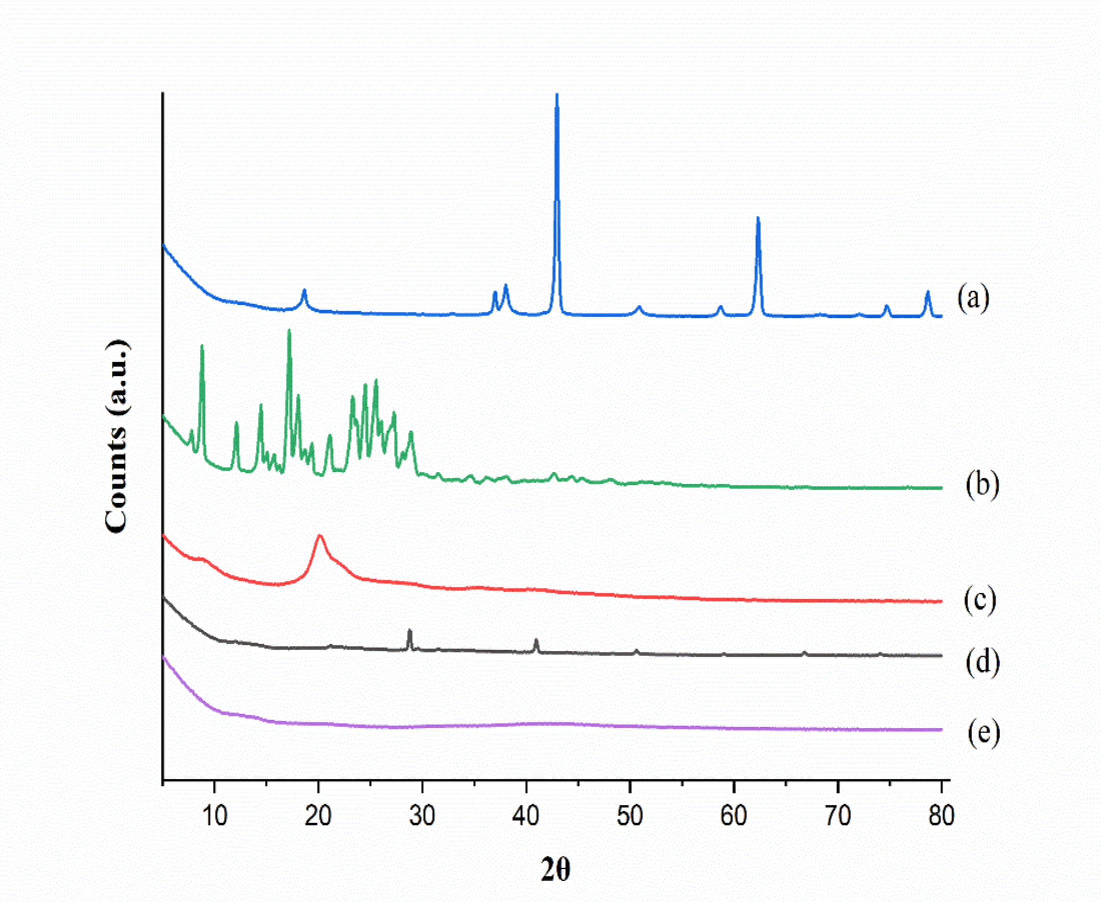

Figure 3.18. XRD patterns of (a) MgO nanoparticles, (b) curcumin, (c) chitosan, (d) carrageenan, and (e) CC/GA2/MO2

Chitosan exhibited a characteristic diffraction peak at 2θ = 20°, and carrageenan presented diffraction peaks at 2θ = 28.5° and 2θ = 40°, indicative of its semicrystalline nature [42, 43]. These peaks reflect the amorphous regions of the polysaccharides, with partial crystallinity stemming from their backbone structure. In the case of MgO-doped chitosan–carrageenan nanoparticles, the broad peaks in this region further broadened and decreased in intensity or almost disappeared, suggesting diminished crystallinity due to nanoparticle formation. This is likely caused by interactions between the polymers, leading to a more entangled and amorphous matrix.

Curcumin displayed multiple sharp peaks in the 7–30° (2θ) range, characteristic of its crystalline structure [44]. However, these peaks were less intense in the curcumin-loaded MgO-doped chitosan–carrageenan nanoparticles, indicating successful encapsulation within the biopolymeric matrix. The reduced peak intensity suggests a loss of long-range order in the crystalline structure of curcumin, indicating its more amorphous or semicrystalline state within the nanoparticle system, which may increase its solubility and controlled release potential.

The XRD pattern of MgO showed sharp characteristic peaks at 36.9°, 38°, 43°, and 62.3° (2θ), corresponding to the cubic phase of MgO [45]. In the curcumin-loaded MgO-doped polyelectrolyte nanoparticles, the intensity of these peaks was significantly reduced or vanished, indicating a fine dispersion of MgO in the biopolymer matrix, which contributes to a reduction in overall crystallinity.

In summary, XRD analysis confirmed the formation of stable MgO-doped chitosan–carrageenan nanoparticles with structural modifications, thus enhancing their suitability for controlled drug delivery applications, particularly curcumin encapsulation and release.

3.3.3.3. Field emission scanning electron microscopy (FESEM) and energy dispersive X-ray spectroscopy (EDX)

The morphological differences between modified and unmodified chitosan–carrageenan (CC) nanoparticles were examined via field emission scanning electron microscopy (SEM) at a magnification of 60000x (Figure 3.19. (a) and (b), respectively). The images revealed distinct structural characteristics influenced by adding glutaraldehyde (GA) as a crosslinking agent and magnesium oxide (MgO) as a dopant in the formulations.

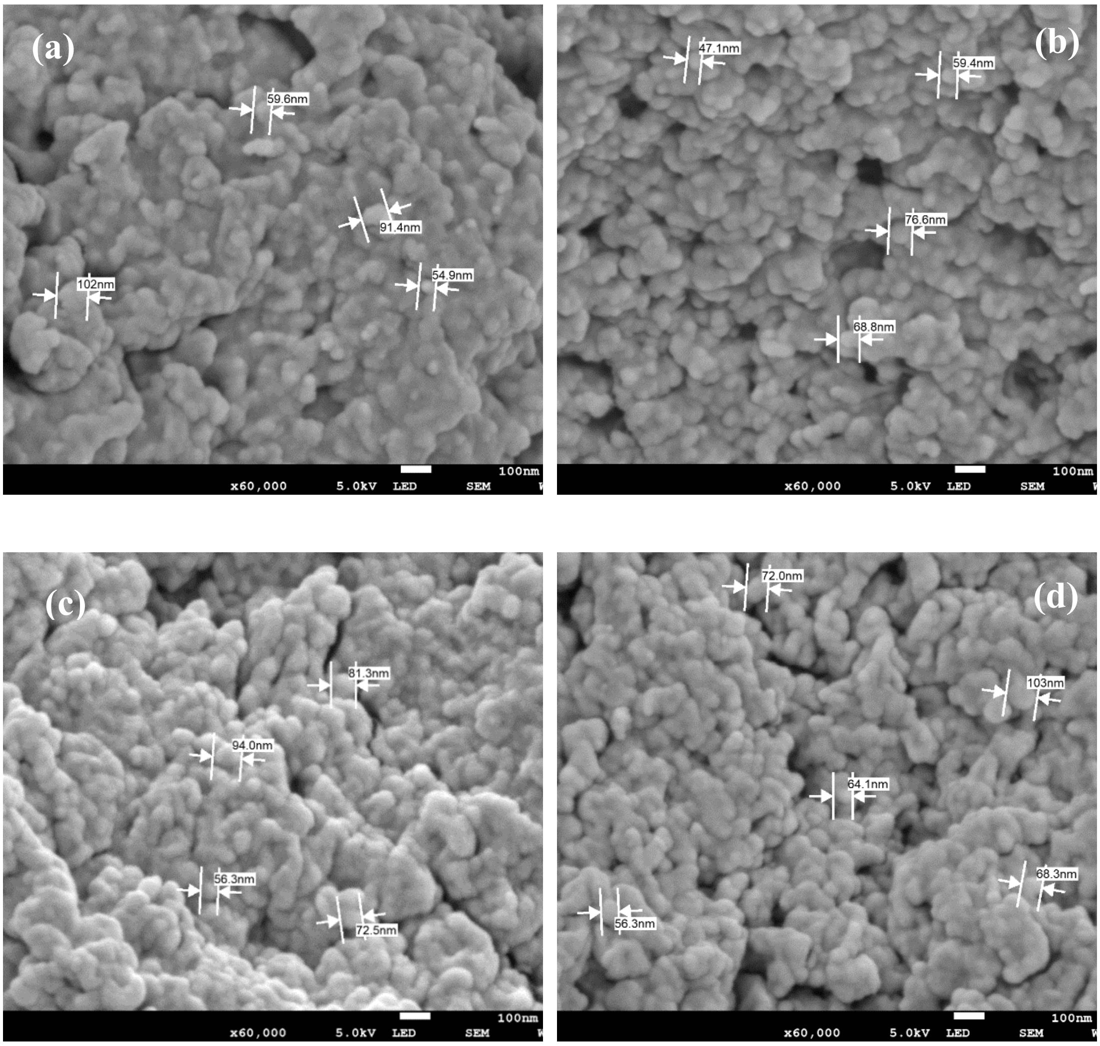

Figure 3.19. FESEM images of (a) CC, (b) CC/GA3, (c) CC/MO3, (d) CC/GA2/MO2

The unmodified CC nanoparticles exhibited a compact and relatively smooth surface with minimal porosity (Figure 3.19. (a)). The particle sizes ranged from approximately 54.9 nm to 102 nm, indicating a dense, layered morphology likely arising from the strong electrostatic interactions between the anionic sulfate groups of carrageenan and the cationic amino groups of chitosan, resulting in a stable, well-integrated matrix. The smooth surface and limited porosity of the CC nanoparticles are reflected in their encapsulation efficiency (67.8%) and drug loading efficiency (51.6%), as this morphology restricts drug accessibility primarily to surface adsorption sites. The high process yield (72.1%) for CC indicates efficient particle formation due to stable chitosan–carrageenan interactions, as observed in similar biopolymer complexes [43]. However, the compact morphology limits the potential for increased drug loading, as evidenced by the moderate drug loading efficiency (LE) and encapsulation efficiency (EE) values.

In the CC/GA3 sample (Figure 3.19. (b)), crosslinking with 7.5% glutaraldehyde resulted in increased roughness and minor porosity. The particle size was slightly smaller, ranging from approximately 47.1 nm to 76.8 nm, indicating a denser and tighter network. The covalent crosslinking introduced by GA likely formed additional bonds between the chitosan and carrageenan chains, enhancing structural stability while decreasing the matrix's flexibility. This correlates with the lower encapsulation efficiency (58.5%) and drug loading efficiency (41.7%) compared to those of the unmodified CC sample, as well as slower release rates, likely due to the restricted diffusion of the drug from the more compact crosslinked network. The process yield also decreased to 65.9%, reflecting the reduced flexibility in particle formation introduced by extensive cross-linking.

The CC/MO3 sample, prepared by doping the CC matrix with 1.5% MgO, exhibited a morphology with a highly rough surface structure (Figure 3.19. (c)). The particle sizes in this sample ranged from 56.3 to 94.0 nm, with visible surface irregularities attributed to the disruption of the compact polymer matrix by MgO particles. MgO likely creates microdomains within the polymeric network, resulting in localised regions of increased surface area. This rough morphology correlates with a higher process yield (74.3%), as the increased surface area may facilitate greater particle formation efficiency. The encapsulation efficiency (61.9%) and drug loading efficiency (40.1%) were slightly lower than those of the unmodified CC due to spatial occupancy by the MgO inside the nanoparticles. The slower drug release rates correlate with the complex spatial arrangement and surface morphology induced by the addition of MgO nanoparticles.

The dual-modified CC/GA2/MO2 sample, containing both 5% GA and 1.0% MgO, displayed a morphology characterised by compact and porous regions (Figure 3.19. (d)). The particle sizes in this sample ranged from 56.3 to 103.0 nm, reflecting the structural contributions of both GA crosslinking and MgO doping. GA crosslinking likely enhances particle stability, forming a rigid polymeric backbone, whereas MgO contributes to surface roughness and porosity, creating a balanced structure that combines stability with increased surface area. This morphology aligns with the intermediate process yield (69.3%) and encapsulation efficiency (59.1%) observed for

CC/GA2/MO2. This dual modification enables enhanced stability and sustained release of encapsulated drug molecules, thereby protecting against burst release. Although the EE and LE values are lower than those of unmodified CCs, the structural balance between rigidity and porosity could support a sustained release profile. This combination of modifications is advantageous for applications that require both high drug-loading capacity and controlled, gradual drug release.

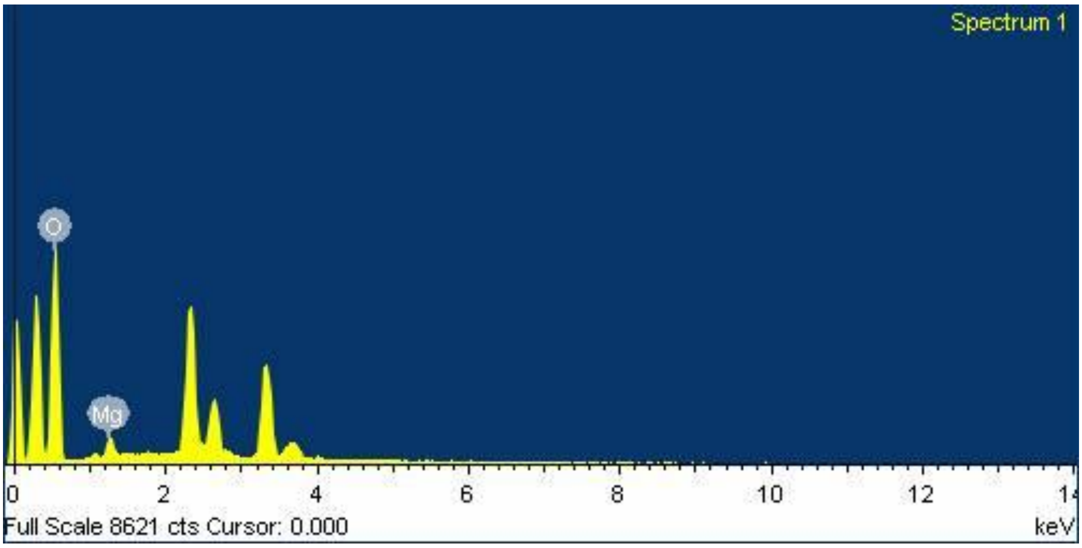

Figure 3.20. EDX pattern of CC/GA2/MO2

Further confirmation of MgO incorporation was obtained through energy-dispersive X-ray (EDX) analysis (Figure 3.20), which revealed the presence of critical elements such as Mg and O from the MgO nanoparticles. This confirms the successful doping of MgO into the chitosan–carrageenan matrix, which is crucial for improving the nanoparticles' structural integrity and drug-release behaviour.

3.3.4. 2-NBDG uptake assay

The 2-NBDG uptake assay was employed to evaluate the effects of curcumin-loaded chitosan–carrageenan nanoparticles, which were prepared by varying the concentration of glutaraldehyde (GA) crosslinking agent and magnesium oxide (MgO), on glucose uptake in L6 myotubes. The assay results indicate that crosslinking density and MgO concentration have a significant influence on cellular metabolic activity.

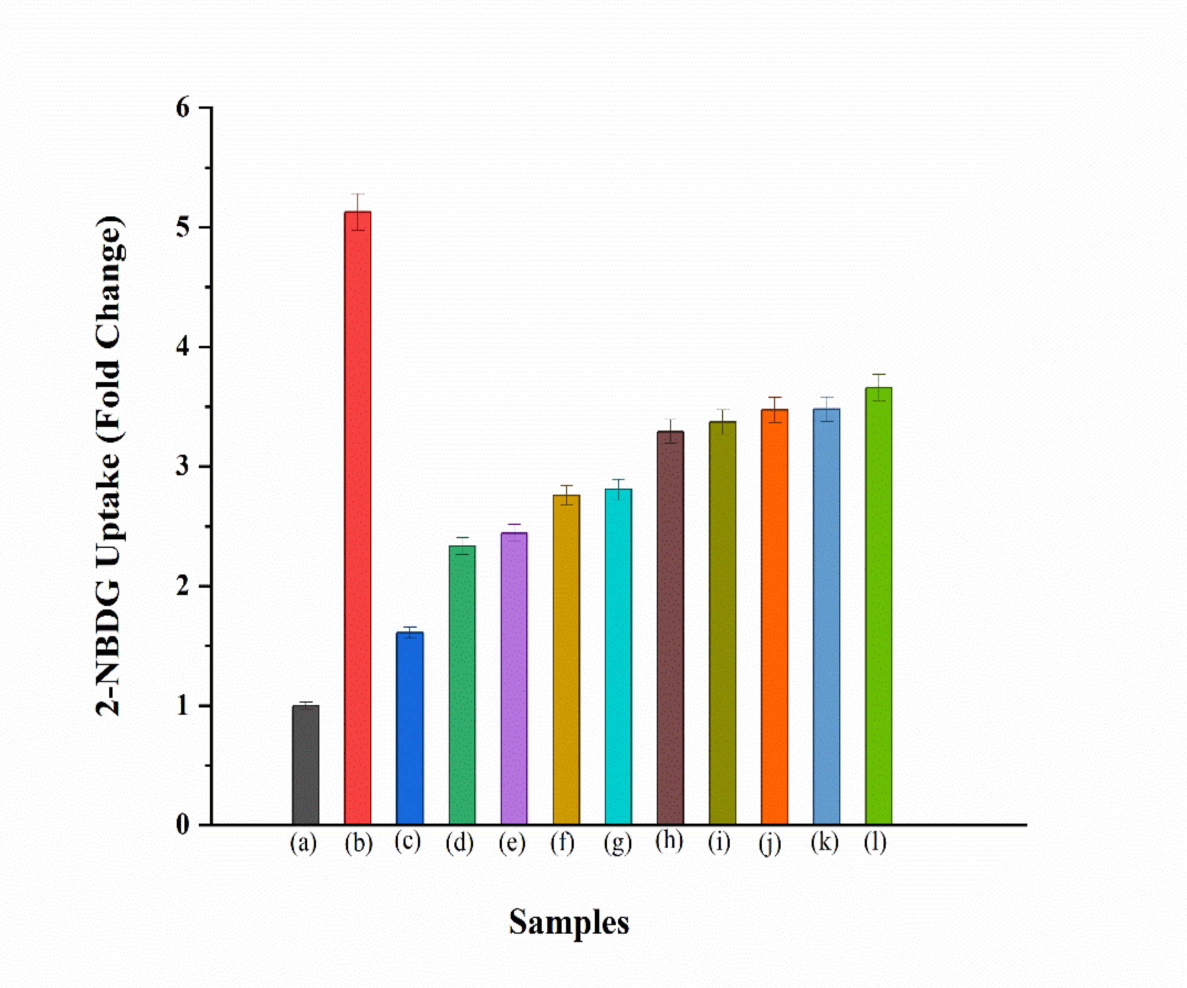

Figure 3.21. Analysis of 2-NBDG uptake by L6 myotubes in response to (a) Control, (b) Insulin, (c) Insulin + Palmitate, (d) CC/GA3, (e) CC/GA2, (f) CC/GA1, (g) CC, (h) CC/GA2/MO2, (i) CC/MO3, (j) CC/MO1, (k) CC/MO2, (l) Curcumin

As expected, untreated control cells presented baseline 2-NBDG uptake, whereas insulin-treated cells presented a marked increase in glucose uptake (Figure 3.21, samples a and b). This positive control confirmed the assay's sensitivity in detecting increased glucose uptake under conditions of enhanced insulin sensitivity. In contrast, cotreatment with insulin and palmitate resulted in significantly reduced glucose uptake (Figure 3.21, sample c), which is consistent with the literature on fatty acid-induced insulin resistance and impaired insulin signalling, thereby reducing glucose uptake in muscle cells.[44, 45] This condition serves as a model of metabolic impairment, providing a comparative basis for assessing the efficacy of nanoparticles in potentially restoring or enhancing glucose uptake.

The curcumin-loaded formulations with higher GA concentrations (Figure 3.21., samples d: CC/GA3 and e: CC/GA2) corresponded to a notable decrease in 2-NBDG uptake relative to insulin-treated cells. This trend aligns with previous studies indicating that increased crosslinking density can result in reduced nanoparticle flexibility and diminished cellular interaction, thereby hindering metabolic function [46]. Reduced flexibility from increased crosslinking density likely limits the nanoparticles' cellular uptake, thereby attenuating curcumin's bioavailability and its potential effects on glucose metabolism. In contrast, nanoparticles with a lower crosslinking density (Fig. 3.21., sample f: CC/GA1) maintained relatively high glucose uptake. These findings suggest that moderate crosslinking levels may support structural stability without significantly compromising cellular uptake. A balanced degree of crosslinking appears to be critical for optimal interactions with cellular membranes, enhancing the metabolic effects of curcumin.

Variations in the MgO concentration within the nanoparticles also affected the uptake of 2-NBDG. NPs with low to moderate MgO concentrations (Figure 3.21, samples j: CC/MO1 and k: CC/MO2) demonstrated relatively high glucose uptake, suggesting that MgO at these levels may positively influence cellular bioactivity. By providing essential magnesium ions, MgO promotes cellular function, which plays a role in glucose metabolism and insulin signalling pathways [47]. These results imply that moderate MgO doping may enhance the therapeutic potential of curcumin-loaded nanoparticles by supporting glucose uptake without adverse cytotoxic effects. Higher MgO doping (Figure 3.21, sample i: CC/MO3) resulted in slightly less glucose uptake, potentially due to the complex's increased rigidity or oxidative stress [48].

The combined formulation with moderate GA crosslinking and MgO doping (Figure 3.21, sample h: CC/GA2/MO2) demonstrated intermediate glucose uptake relative to both high and low concentrations of GA and MgO. This sample’s glucose uptake, while lower than that of the insulin-and curcumin-alone treatments, was greater than that of the formulations with higher GA or MgO concentrations alone. This result suggests a potential synergistic effect of moderate crosslinking and doping levels, allowing for sufficient structural stability and bioactivity without excessive cytotoxicity. These findings suggest that achieving a balanced level of crosslinker and dopant can result in a formulation that exhibits both desirable stability and metabolic benefits.

Curcumin alone (Figure 3.21, sample l) increased glucose uptake. Curcumin modulates inflammatory pathways and antioxidant responses, alleviating cellular stress and enhancing glucose uptake. This result aligns with the hypothesis that curcumin can positively impact glucose metabolism even when it is delivered without additional modifications, highlighting its therapeutic potential in metabolic disorders [49].

Overall, the 2-NBDG uptake results suggest that curcumin-loaded chitosan–carrageenan nanoparticles, particularly those with lower GA crosslinking and moderate MgO doping, enhance glucose uptake in L6 myotubes. The optimal balance of GA and MgO is essential to maintain biocompatibility and maximise glucose uptake.

3.3.5. Cell viability assay

The cytotoxicity of the curcumin-loaded chitosan–carrageenan nanoparticles modified with various concentrations of glutaraldehyde (GA) and magnesium oxide (MgO) nanoparticles was assessed via the MTT assay in cell lines. Cell viability was quantified relative to control cells (100% viability) and measured spectrophotometrically at 570 nm. The untreated control cells demonstrated 100% viability and served as the baseline for comparison. All the samples exhibited good biocompatibility, with no significant cytotoxicity observed across the tested concentrations.

The chitosan-carrageenan (CC) formulation consistently exhibited high cell viability across all the tested concentrations, indicating minimal cytotoxicity. These findings support the biocompatibility of chitosan and carrageenan as safe, biodegradable materials for drug delivery applications. These materials are well regarded for their low toxicity profiles, aligning with studies showing high tolerance in cellular systems owing to the nontoxic, degradable nature of the polysaccharide-based matrix [13].

Cell viability exhibited a slight, concentration-dependent decline in formulations containing MgO, with the highest MgO-containing sample (CC/MO3) showing a more noticeable reduction. This trend is likely due to the oxidative stress effects of MgO, which can lead to the production of reactive oxygen species (ROS) and moderate cytotoxic effects at higher doses [50]. However, cell viability remained high at lower MgO concentrations, as seen in CC/MO1, indicating that moderate MgO levels provide structural reinforcement without significantly compromising cell health. This finding is consistent with the findings of Marapureddy and Thareja, who reported that nanofiller materials can enhance the mechanical properties of nanoparticles while maintaining their biocompatibility [51].

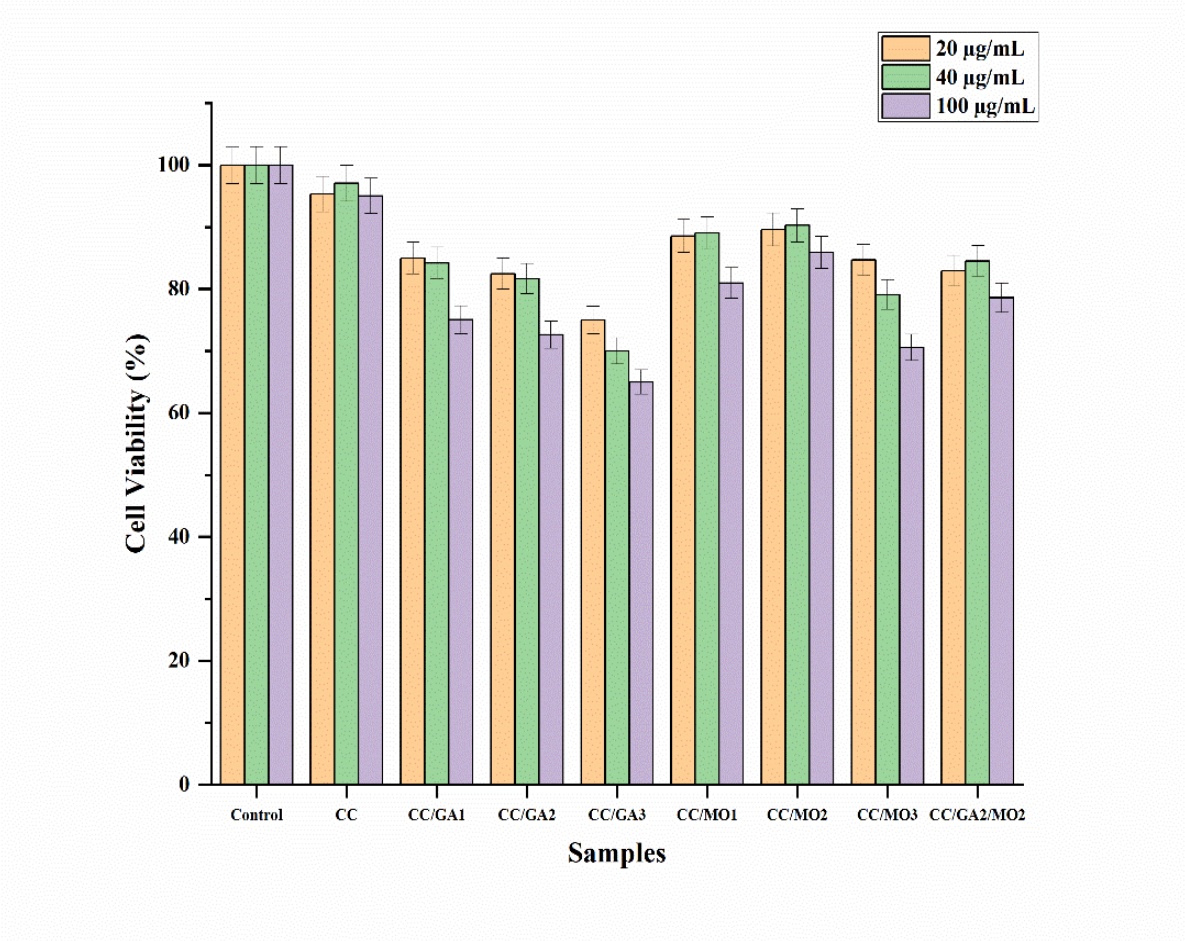

Figure 3.22. Cytotoxicity assay performed for the curcumin-loaded systems with varying concentrations of GA and MgO nanoparticles

The formulations crosslinked with GA resulted in a more pronounced reduction in cell viability, especially at higher GA levels. Although GA effectively controls drug release by increasing the structural rigidity of nanoparticles, its reactivity can lead to reduced cell viability due to residual GA within the matrix [21]. Interestingly, at lower concentrations, GA-crosslinked nanoparticles (CC/GA1) maintained cell viability above 80%, suggesting that minimal GA usage is viable for stabilising nanoparticles while preserving biocompatibility. Our results align with those of the study by Oliveira et al., which demonstrated that careful modulation of GA levels in biopolymer systems does not adversely affect cell viability [22].

The formulation combining both MgO and GA (CC/GA2/MO2) resulted in a moderate and dose-dependent decrease in cell viability across concentrations, highlighting a cumulative cytotoxic effect. This dual modification likely reinforces the nanoparticle matrix structure, thus effectively regulating curcumin release.

These results highlight the importance of optimising both the GA crosslinker and MgO dopant levels in curcumin-loaded chitosan–carrageenan nanoparticles to achieve minimal cytotoxicity and maintain therapeutic efficacy. Low concentrations of GA and MgO appear to be optimal for ensuring high cell viability, suggesting a formulation with the potential for safe and effective curcumin delivery in therapeutic contexts.

3.4. DEVELOPMENT OF A pH-RESPONSIVE SOY FLOUR–MONTMORILLONITE–MAGNESIUM OXIDE COMPLEX FOR SUSTAINED RELEASE OF CURCUMIN IN ANTIDIABETIC THERAPY

3.4.1. Process yield, drug loading and drug encapsulation efficiency

The nanoparticle formulations' process yield (%) was determined using the equation provided in section 2.2.7 (Chapter 2). Table 3.4. summarises the yields of various polymer systems developed for the delivery of curcumin, along with the impact of varying MgO, MMT, and glutaraldehyde (GA) concentrations on the system's characteristics. Notably, variations in the GA, MMT and MgO concentrations did not significantly impact the overall process yield.

Increasing the MgO concentration negatively affected drug loading. MgO’s strong ionic character and large surface area lead to higher interaction with soy flour, leaving less space for drug entrapment.9 Similar to drug loading, the encapsulation efficiency also decreased with increasing MgO concentration. The interaction between MgO and the drug could restrict the availability of Curcumin for encapsulation due to adsorption onto the MgO surface. Additionally, MgO can also facilitate some crosslinking, providing mechanical strength to the polymer system and reducing the amount of drug entrapment by imparting rigidity and compactness to the polymer complex structure [20].

As the MMT content increased, the encapsulation and drug loading efficiency decreased. This effect can be attributed to the interaction between the –OH groups of MMT's silicate layers and the $–NH_2$ groups of soy flour, causing the polymer chains to extend [21]. The silicate layers in MMT restrict the free movement of intercalated polymer chains, forming a porous structure during dehydration, with multiple small channels running from the interior to the outer surface of the complex. As a result, part of the drug could diffuse out of the complex into the surrounding medium, lowering both encapsulation efficiency and drug loading efficiency [22,23]. The absence of MMT layers in the MMT-free crosslinked complex eliminated the hindrance observed in those with MMT. Additionally, incorporating MMT might reduce the available space for drug accommodation, leading to a decline in encapsulation and loading efficiency.

Similarly, an increase in GA concentration was found to reduce encapsulation efficiency. The aldehyde groups of GA react with the amino groups of SF, and the increase in GA concentration restricts the free movement of polymer chains, thereby promoting the formation of a porous structure [24]. This structure provides channels through which curcumin can migrate from the nanoparticle core to the preparation medium. Moreover, the interaction between GA and the polymer network results in a more compact and rigid structure, reducing the free volume within the polymer matrix [25]. As a consequence, both encapsulation and drug loading efficiencies were decreased.

Table 3.4. Preparation of Curcumin-loaded MgO doped SF–MMT complex with different concentrations of MgO nanoparticles.

Sample code	SF % w/v (amount in g in 50 mL water)	MgO nanoparticles % w/w w.r.t SF (amount in g)	Process yield (%)	Encapsulation efficiency (%)	Drug loading efficiency (%)
A0	1 (0.5)	0.0 (0.0000)	84.72 (±0.02)	73.50 (±0.04)	89.14 (±0.01)
A1	1 (0.5)	0.4 (0.0020)	86.20 (±0.01)	66.21 (±0.01)	86.62 (±0.03)
A2	1 (0.5)	0.7 (0.0035)	87.15 (±0.02)	53.23 (±0.03)	85.27 (±0.03)
A3	1 (0.5)	1.0 (0.005)	88.14 (±0.02)	46.56 (±0.01)	84.24 (±0.04)

Curcumin = 0.05 g, Tween 80 = 0.015 mL, MMT= 0.005 g, GA= 5μL.

[*] Each value and the standard deviation in parentheses represent the average of five readings.

Table 3.5. Preparation of Curcumin-loaded MgO doped SF–MMT complex with different concentrations of MMT nano-clay

Sample code	SF % w/v (amount in g in 50 mL water)	MMT % w/w w.r.t. SF (g in 50 mL water)	Process yield (%)	Encapsulation efficiency (%)	Drug loading efficiency (%)
B0	1 (0.5)	0 (0.000)	81.73 (±0.01)	49.17 (±0.01)	86.57 (±0.01)
B1	1 (0.5)	1.0 (0.005)	88.14 (±0.02)	46.56 (±0.01)	84.24 (±0.04)
B2	1 (0.5)	3.0 (0.015)	78.23 (±0.04)	37.15 (±0.02)	81.83 (±0.04)
B3	1 (0.5)	5.0 (0.025)	87.81 (±0.02)	31.13 (±0.01)	79.36 (±0.03)

Curcumin = 0.05 g, Tween 80 = 0.015 mL, MgO nanoparticles = 0.005g, GA= 5µL.

*Each value and the standard deviation in parentheses represent the average of five readings.

Table 3.6. Preparation of Curcumin-loaded MgO doped SF–MMT complex with different concentrations of cross-linker

Sample code	SF % w/v (amount in g in 50 mL water)	GA % v/w w.r.t SF (amount in mL)	Process yield (%)	Encapsulation efficiency (%)	Drug loading efficiency (%)
C0	1 (0.5)	0 (0.000)	82.41 (±0.02)	64.25 (±0.02)	89.98 (±0.01)
C1	1 (0.5)	0.3 (0.0015)	88.72 (±0.01)	63.83 (±0.01)	89.65 (±0.01)
C2	1 (0.5)	0.5 (0.0025)	79.51 (±0.04)	61.36 (±0.01)	87.19 (±0.02)
C3	1 (0.5)	0.7 (0.0035)	77.34 (±0.03)	59.02 (±0.02)	86.86 (±0.03)
C4	1 (0.5)	1.0 (0.0050)	88.14 (±0.02)	46.56 (±0.01)	84.24 (±0.04)

Curcumin = 0.05 g, Tween 80 = 0.015 mL, MgO nanoparticles = 0.005g, MMT= 0.005 g.

*Each value and the standard deviation in parentheses represent the average of five readings.

3.4.2. *In vitro* drug release study

The study investigated the *in vitro* drug release profiles of curcumin from soy flour-based drug delivery systems with varying concentrations of MgO nanoparticles and montmorillonite (MMT) clay under simulated intestinal (pH 7.4) and gastric (pH 1.2) conditions. The inclusion of MgO and MMT aimed to modulate the matrix structure and, consequently, the release behaviour of the hydrophobic drug curcumin.

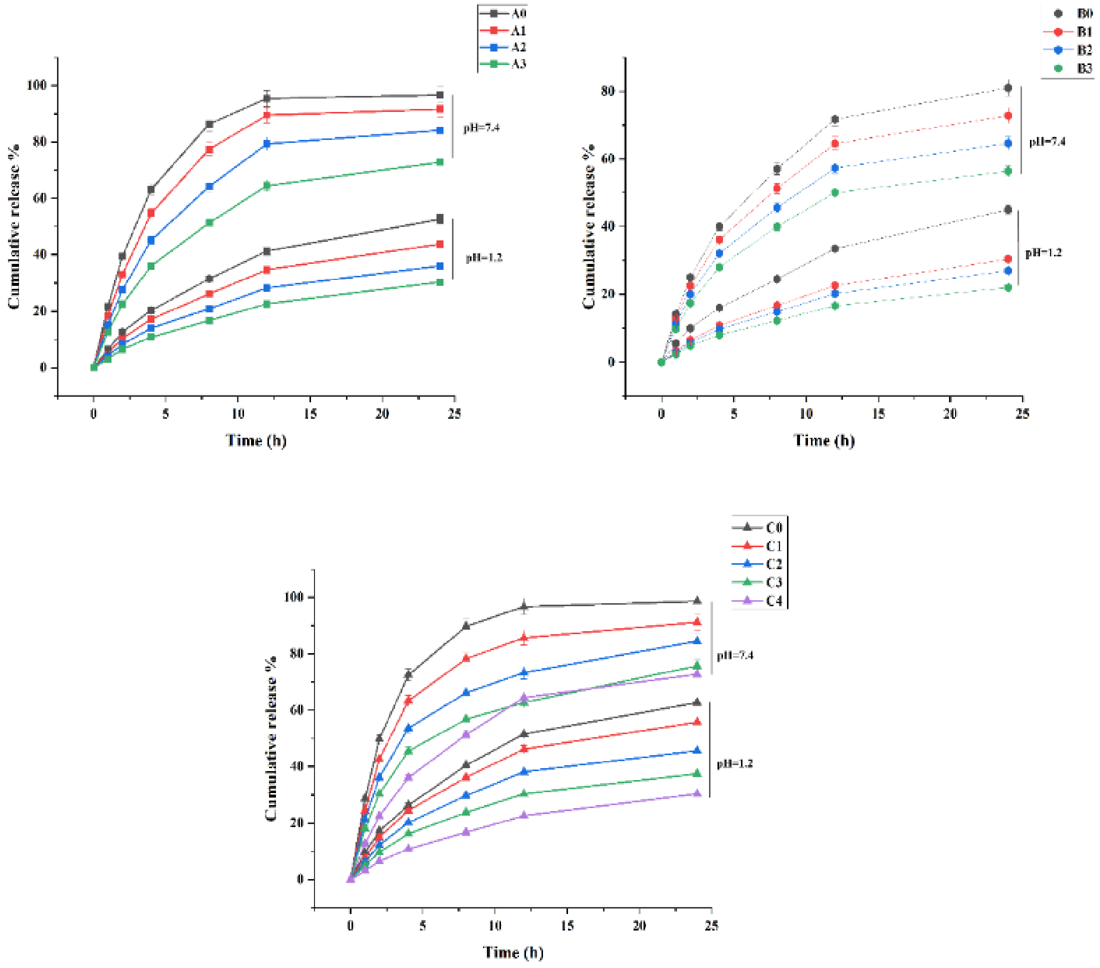

Figure 3.23. The cumulative drug release profile for different samples at pH =1.2 and pH=7.4

At pH 7.4, a clear trend of decreasing drug release was observed with increasing concentrations of MgO. The sample without MgO (A0) exhibited the highest release, demonstrating less matrix restriction and more favourable conditions for curcumin diffusion. In contrast, increasing MgO concentrations (A1 to A3) resulted in progressively lower release rates, highlighting the role of MgO in enhancing matrix density and reducing drug permeability. This was mirrored in the B series, where varying MMT concentrations decreased, with B0 releasing the most drugs and B3 the least.

At pH 1.2, the release rates were universally lower across all formulations, reflecting the impact of the acidic environment on both the matrix and the solubility of curcumin. Notably, the decrease was more pronounced in formulations with higher concentrations of additives, which further restricted the swollen state of the hydrogel, limiting drug release more significantly.

The C series further investigated the effect of varying glutaraldehyde (GA) concentrations, used as a cross-linker, on drug release. The introduction of GA from C0 to C4 resulted in a marked decrease in drug release at both pH levels. The cross-linking introduced by GA produced a tighter and more rigid hydrogel network, significantly impeding the diffusion of curcumin out of the matrix. The most cross-linked sample (C4) exhibited the lowest release rates, illustrating the profound impact of chemical cross-linking on controlling drug release.

The differential release patterns observed at pH 7.4 versus pH 1.2 across all series underscore the importance of environmental pH in the design and application of drug delivery systems. The lower release rates at pH 1.2 indicate the matrix’s limited swelling capabilities under acidic conditions, which is critical for releasing hydrophobic drugs like curcumin. At lower pH, most of the carboxylate anions of SF become protonated, leading to decreased swelling. Whereas, some of the carboxylate (COO-) groups become ionised at higher pH. Hence, the repulsion between the COO- groups facilitate the swelling [26]. This pH-responsive behaviour suggests that such hydrogel systems could be beneficial in targeted drug delivery applications, where the release environment's pH could trigger or modulate drug release [27]. Adjusting the concentration of these additives enables the fine-tuning of the release rates of hydrophobic drugs for specific therapeutic applications. Furthermore, the observed pH-dependent release behaviour offers additional avenues for drug-controlled release, potentially enhancing the efficacy and safety of curcumin treatment regimens.

3.4.3. Characterisation

3.4.3.1. Fourier transform infrared spectroscopy

Fourier Transform Infrared Spectroscopy (FTIR) was used to investigate the chemical interactions between Soy flour, Curcumin, MgO nanoparticles, and MMT nano-clay. The spectra of the individual components and the formulation were recorded, and the characteristic absorption bands were analysed to identify any potential chemical interactions or structural changes due to the formulation.

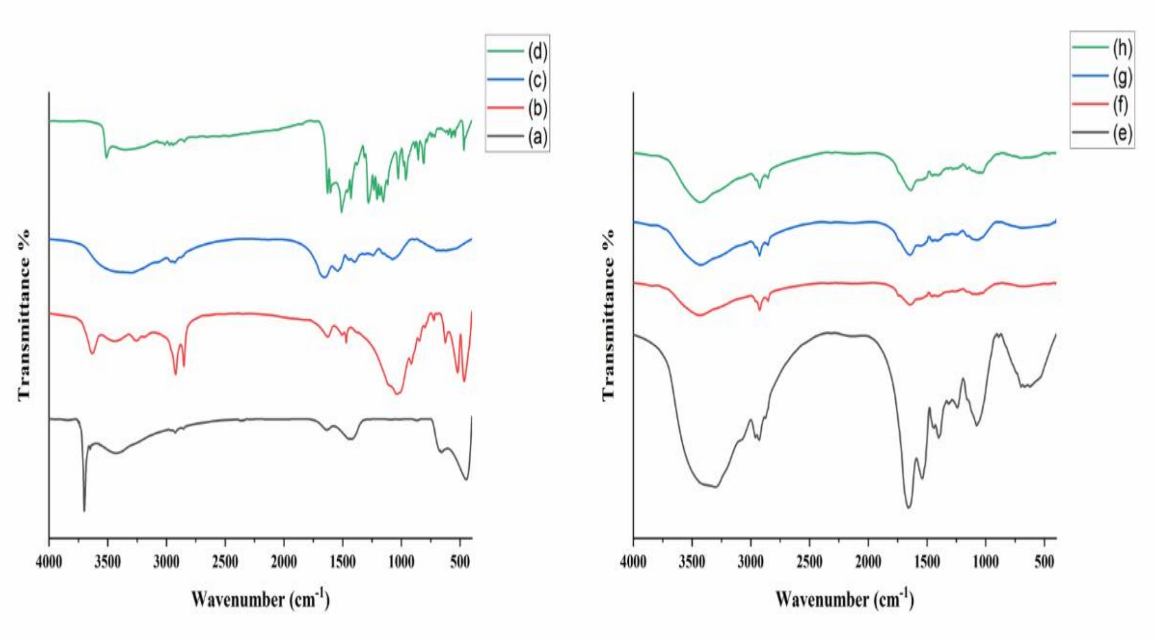

Figure 3.24. FTIR spectra of (a) MgO nanoparticles, (b) MMT nano-clay, (c) Soy Flour, (d) Curcumin, (e) B0, (f) A0, (g) C0, (h) A3/B1/C4

The spectrum of MgO nanoparticles (Figure 3.24.a) exhibited a broad peak around 3600 cm^{-1}, attributable to hydroxyl groups, suggesting surface-adsorbed water molecules. The sharp peaks near 500-600 cm^{-1} indicate Mg-O stretching vibrations, confirming the presence of MgO [28]. In the spectrum for MMT nano-clay (Figure 3.24.b), distinct peaks at 3620 cm^{-1} and 3420 cm^{-1} were observed, corresponding to OH stretching of Al-OH groups. The strong peak around 1030 cm^{-1} represents Si-O stretching, a characteristic of silicate materials, indicating the presence of intact silicate layers in MMT [29]. In the soy flour spectrum (Figure 3.24.c), a broad absorption band in the wavelength range 3350-3450m was due to the hydrogen-bonded -OH stretching and NH_2 asymmetric stretching vibrations. Further, peaks at 1650 cm^{-1} and 1530 cm^{-1} were identified as amide I (C=O stretching) and amide II (N-H bending) bands, respectively, indicative of the protein content in soy flour [30]. The amide III band was also found to appear at 1250cm^{-1} (C-N stretching) due to the presence of glutamic acid in soy flour

[31]. The spectrum for curcumin (Figure 3.24.d) showed peaks at 3500 cm^{-1} for OH groups, 1625 cm^{-1} for C=O stretching, and 1505 cm^{-1} for benzene ring vibrations, consistent with its molecular structure [32].

The FTIR spectra confirm the successful integration of MgO and MMT into the soy matrix alongside entrapped curcumin. Soy flour's amide I and amide II peaks remain discernible in every formulation, while key signals from MMT (Si–O–Si stretch) and MgO (metal–oxide stretch) appear in the doped samples. Curcumin's characteristic β-diketone/carbonyl region partially overlaps with the amide bands but can still be identified as a shoulder or slight shift in intensity. Crosslinking (GA) induces broader O–H/N–H stretching bands and minor shifts in amide regions, indicative of new imine linkages and enhanced matrix rigidity. These FTIR results highlight the composite's multi-component structure and the interplay between crosslinking and filler incorporation on the proteinaceous network.

3.4.3.2. X-ray diffraction study

Powder X-ray diffraction (P-XRD) was employed to gain insights into the structural properties and confirm the successful encapsulation of curcumin delivery in the polymeric nanoparticles.

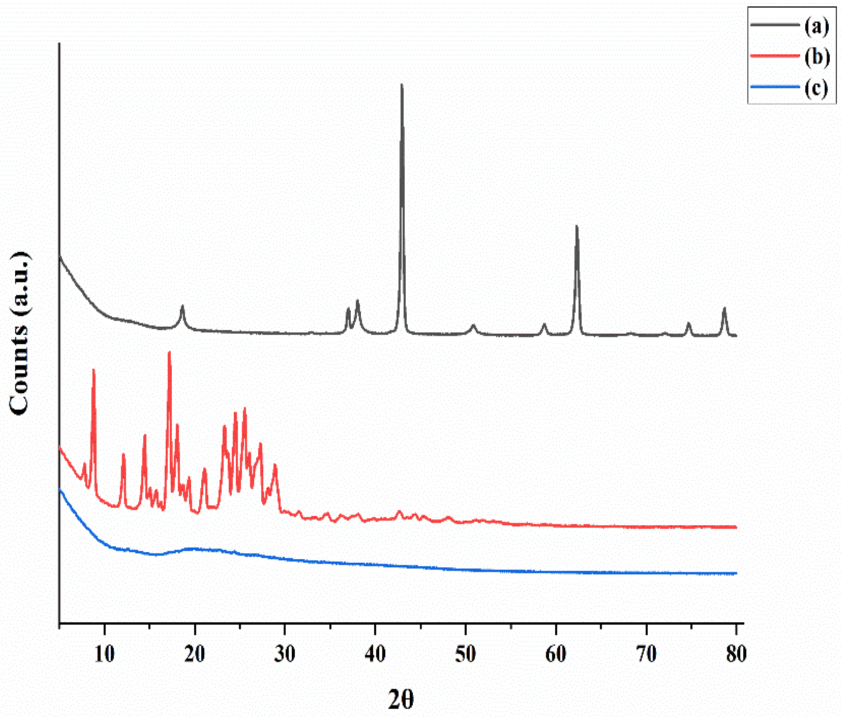

Figure 3.25. XRD pattern of (a) MgO nanoparticles, (b) Curcumin, (c) A3/B1/C4.

The X-ray diffraction pattern of MgO nanoparticles (Figure 3.25.a) reveals distinct sharp peaks at 2θ values typically around 36.8°, 42.9°, and 62.3°. These peaks correspond to the (111), (200), and (220) planes of cubic MgO [33]. The sharpness of these peaks signifies a high degree of crystallinity and purity of the MgO nanoparticles, suggesting a minimal presence of structural defects or impurities. Curcumin exhibited characteristic peaks at 2θ values of approximately 8.5°, 14.8°, 17.1°, and 23.4° in the XRD spectrum (Figure 3.25.b). These peaks align with curcumin's known crystalline form, indicating its stable monoclinic phase with well-defined crystal planes [34]. The high intensity and narrow width of these peaks suggest that the curcumin used is in its highly crystalline and purest form, which is essential for maintaining its stability and bioactivity**.** The XRD pattern for the curcumin-loaded MgO-doped soy flour-MMT nanoparticles (Figure 3.25.c) displays a significantly altered profile with noticeable peak broadening and reduced intensity compared to the pure components. The characteristic peaks of MgO are subdued, and a broad hump in the range of 15° to 25° is observable, suggesting a highly amorphous structure or smaller crystal domains. This amorphous nature is beneficial for drug delivery applications as it enhances the solubility and bioavailability of curcumin, and the encapsulation of the drug in the polymer matrix improves its stability [35]. The reduced crystallinity and presence of amorphous regions indicate a matrix that could potentially control the release of curcumin more effectively than its crystalline counterpart.

3.4.3.3. Field emission scanning electron microscopy (FESEM) study

FESEM imaging was employed to examine the structure of curcumin-loaded MgO-doped soy flour–MMT complexes, which were formulated with varying concentrations of MgO, montmorillonite (MMT), and glutaraldehyde (GA). These images provided crucial insights into the physical changes within the hydrogel matrices due to different additive concentrations and their potential effects on drug release behaviour. The surface of unmodified SF was smooth. C0 (0% GA) showed a rougher surface than SF's. This increased roughness can be attributed to the interaction of MgO with SF. The matrix surface in A0 (0% MgO) showed more roughness and porosity. B0 (0% MMT) showed slightly more porosity and texture. The A3/B1/C4 image illustrates the pronounced effect of MgO and MMT doping, as well as GA crosslinking, on the morphology compared to the unmodified SF image. The presence of MgO nanoparticles disrupts matrix uniformity, suggesting a potential for these particles to influence mechanical properties and drug release pathways by creating physical barriers to drug diffusion [36]. MMT's layered structure contributes to matrix densification, which could benefit applications requiring controlled, slow drug release. The addition of MMT resulted in a more compact and cluttered matrix, suggesting that MMT may restrict drug release by enhancing matrix rigidity and reducing porosity [37]. The cross-linking introduced by GA was visible as a more coherent and compact matrix, which would logically impede curcumin diffusion, correlating with the observed decrease in drug release rates [38].

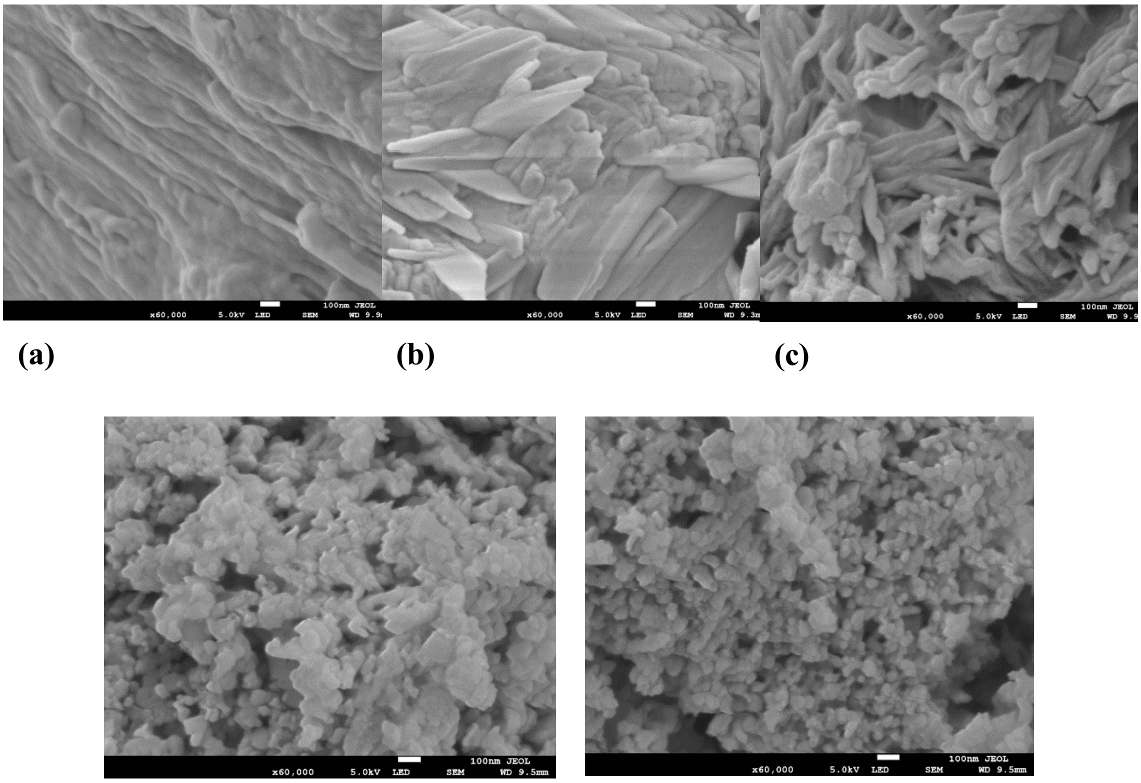

(a) **(b)** **(c)**

(d) **(e)**

Figure 3.26. FESEM images of (a) SF, (b) C0, (c) A0, (d) B0, (e) A3/B1/C4

The FESEM analysis effectively illustrated how incorporating MgO, MMT, and GA alters the structure of soy flour-based matrices. Each additive plays a distinct role in modulating the release profile of curcumin, confirming the hypothesis that matrix structure directly influences drug release dynamics.

3.4.4. 2-NBDG uptake assay

The 2-NBDG uptake assay evaluated the glucose uptake potential of curcumin-loaded MgO-doped glutaraldehyde-crosslinked soy flour-MMT complexes. The assay results revealed that the crosslinking density and MgO concentration significantly influenced cellular metabolic activity. Untreated control cells showed baseline 2-NBDG uptake, while insulin-treated cells exhibited a marked increase in glucose uptake, confirming the assay's sensitivity. In contrast, formulations with higher GA concentrations (e.g., C3 and C4) demonstrated reduced glucose uptake compared to those with lower crosslinking densities (e.g., C0 and C1), consistent with the observation that increased crosslinking density reduces nanoparticle flexibility and limits cellular interaction [39]

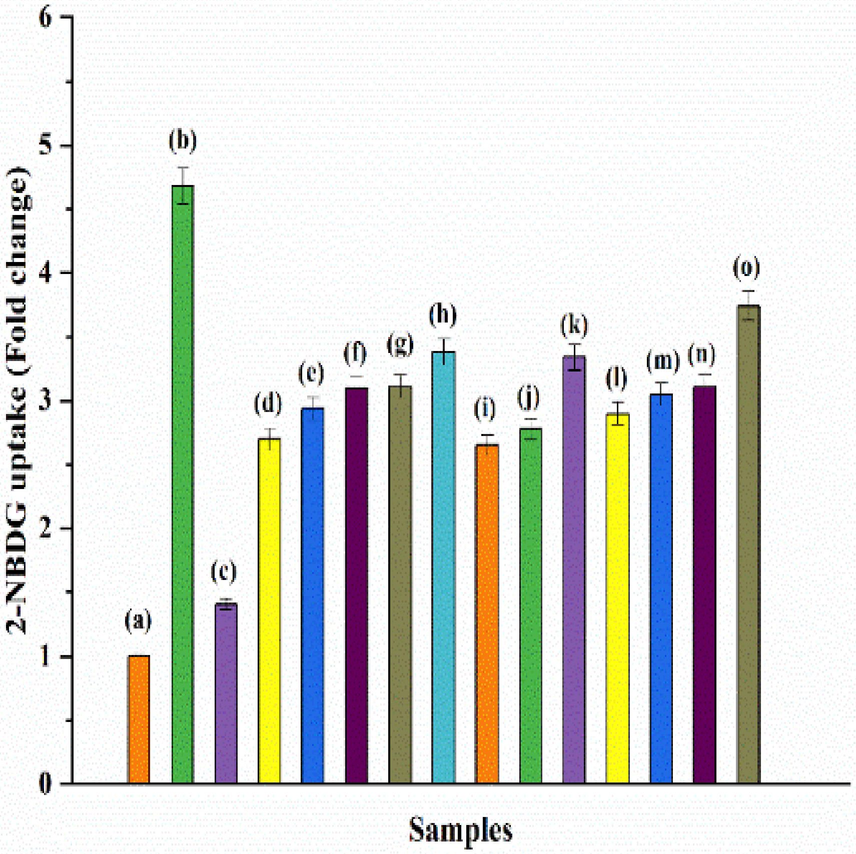

Figure 3.27. Analysis of 2-NBDG uptake by L6 myotubes in response to (a) Control, (b) Insulin, (c) Insulin + Palmitate, (d) A3/B1/C4, (e) C3, (f) C2, (g) C1, (h) C0, (i) B3, (j) B2, (k) B0, (l) A2, (m) A1, (n) A0, (o) Curcumin

Similarly, samples with no MgO doping (e.g., A0) exhibited higher glucose uptake, likely due to the absence of structural rigidity. Low-to-moderate MgO doping (e.g., A1) resulted in relatively high glucose uptake, suggesting that moderate MgO levels enhance cellular bioactivity by providing essential magnesium ions that play a role in glucose metabolism [40]. However, higher MgO concentrations (e.g., A3) reduced glucose uptake, likely due to increased matrix rigidity or oxidative stress [41] The inclusion of MMT also influenced glucose uptake, with samples containing lower MMT concentrations (e.g., B0) demonstrating better glucose uptake than those with higher MMT levels (e.g., B3). The compact structure induced by MMT's silicate layers likely impeded curcumin release and cellular interaction [42].

Combined formulations with high concentrations of GA, MgO, and MMT (e.g., A3/B1/C4) displayed significantly reduced glucose uptake, consistent with the cumulative effects of matrix rigidity and reduced nanoparticle flexibility. Curcumin alone enhanced glucose uptake, aligning with its known antioxidant and anti-inflammatory effects that improve glucose metabolism [43]

These findings suggest that curcumin-loaded formulations with balanced GA and MgO concentrations promote glucose uptake, whereas excessive crosslinking or dopant levels reduce nanoparticles' cellular interaction.

3.4.5. Cell viability assay

Cell viability was measured spectrophotometrically at 570 nm and quantified relative to control cells, which exhibited 100% viability and served as a baseline for comparison. The results have underscored the significant influence of MgO, MMT, and glutaraldehyde concentrations on cell viability.

The control sample (C0), containing no additives, demonstrated the highest viability, nearing the 100% baseline. This indicates high cell viability and confirms the inherent biocompatibility of the soy flour matrix. This finding aligns with previous research, which has noted the low toxicity profiles of soy-based systems, particularly in biopolymeric applications where natural compatibility is crucial [44].

A concentration-dependent decline in cell viability was observed with the introduction of MgO (samples A1 through A3). The sample with the highest MgO content (A3) exhibited a greater reduction in cell viability, a trend likely attributed to the oxidative stress effects associated with MgO nanoparticles. These results are consistent with the literature, indicating that MgO can induce reactive oxygen species (ROS) production, which, at higher doses, compromises cellular integrity [45].

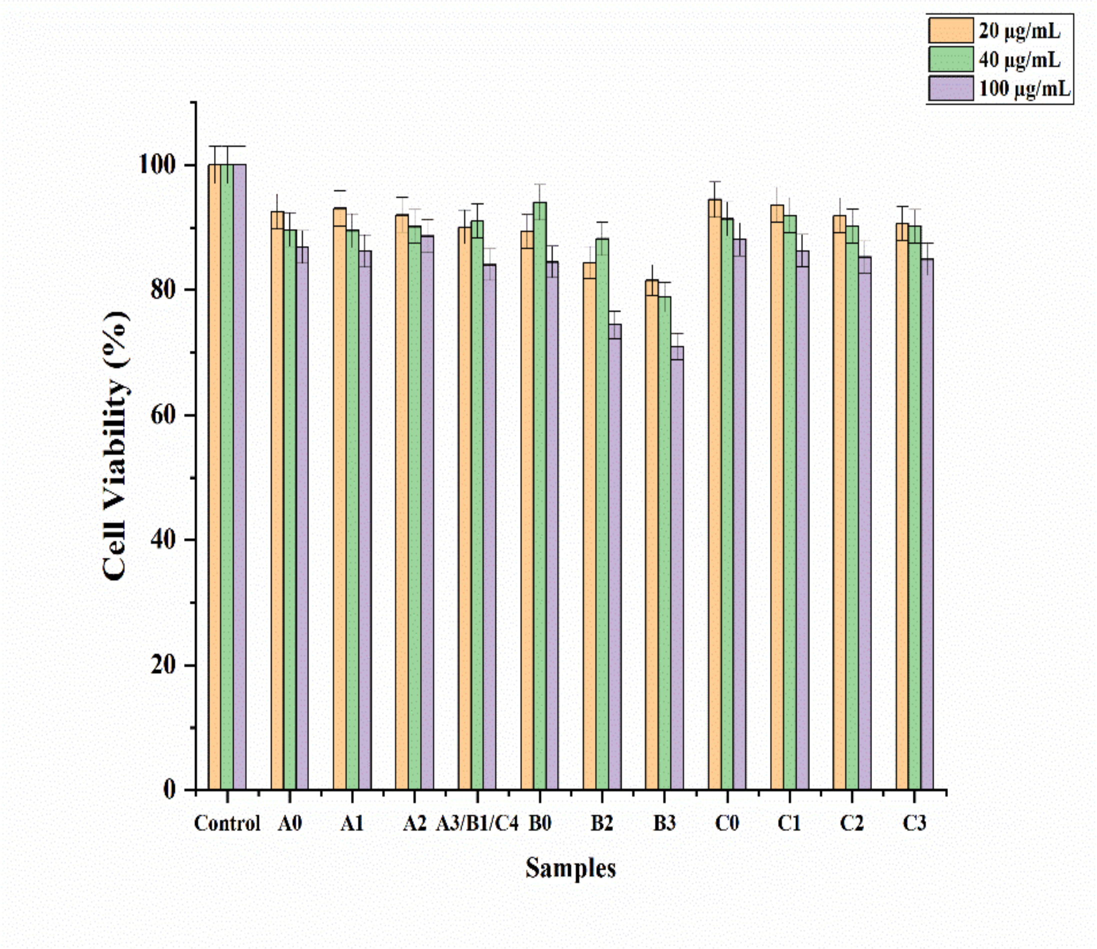

Figure 3.28. Cytotoxicity assay performed for the curcumin-loaded systems with varying concentrations of GA, MMT and MgO nanoparticles

Similarly, the incorporation of MMT (samples B0 through B3) also demonstrated a dose-dependent decrease in cell viability. The increased concentration of MMT appears to enhance the structural rigidity of the nanoparticles, consequently restricting the cellular uptake due to the matrix's densification. These findings suggest that higher filler content in biopolymeric systems can impede biocompatibility due to alterations in mechanical properties and barrier effects [46].

While GA effectively enhances the structural integrity of nanoparticles, facilitating controlled drug release, its reactivity can lead to cytotoxic effects, particularly at elevated concentrations. The observed decrease in cell viability with increasing GA levels aligns with existing research [47]. Crosslinkers can stabilise drug delivery systems, but must be meticulously balanced to avoid adverse cytotoxic effects.

The combination of MgO, MMT, and GA in sample A3/B1/C4 comparatively lowered cell viability in this study, illustrating the cumulative cytotoxic effects when all three components are at their highest concentration. This outcome highlights the need for careful optimisation of each additive to mitigate adverse interactions and maintain the therapeutic efficacy of the drug delivery system.

These findings highlight the complex interplay between nanoparticle composition and cell viability. While each component—MgO, MMT, and GA—can individually enhance certain aspects of drug delivery, their combined effects at high concentrations can significantly diminish biocompatibility. Future formulations must consider the balance between structural benefits and potential cytotoxicity to optimise therapeutic outcomes in clinical applications.

3.5. REFERENCES

[1] Yuan, Y., Chesnutt, B.M., Utturkar, G., Haggard, W.O., Yang, Y., Ong, J.L., Bumgardner, J. D., The effect of cross-linking of chitosan microspheres with genipin on protein release. *Carbohydr Polym,* 68:561–567, 2007.

[2] Hua, S., Yang, H., Wang, A., A pH-sensitive nanocomposite microsphere based on chitosan and montmorillonite with in vitro reduction of the burst release effect. *Drug Dev Ind Pharm,* 36:1106–1114, 2010.

[3] Assaad, E., Wang, Y. J., Zhu, X. X., Mateescu, M. A., Polyelectrolyte complex of carboxymethyl starch and chitosan as drug carrier for oral administration. *Carbohydr Polym,* 84:1399–1407, 2011.

[4] Sağlam, D., Venema, P., de Vries, R., van der Linden, E, The influence of pH and ionic strength on the swelling of dense protein particles. *Soft Matter,* 9:4598, 2013.

[5] Iman, M., Maji, T. K., Effect of crosslinker and nanoclay on starch and jute fabric based green nanocomposites. *Carbohydr Polym,* 89:290–297, 2012.

[6] Nastaj, J., Przewłocka, A., Rajkowska-Myśliwiec, M., Biosorption of Ni(II), Pb(II) and Zn(II) on calcium alginate beads: equilibrium, kinetic and mechanism studies. *Polish Journal of Chemical Technology,* 18:81–87, 2016.

[7] Ikuta, N., Tanaka, A., Otsubo, A., Ogawa, N., Yamamoto, H., Mizukami, T., Arai, S., Okuno, M., Terao, K., Matsugo, S., Spectroscopic Studies of R(+)-α-Lipoic Acid—Cyclodextrin Complexes. *Int J Mol Sci,* 15:20469–20485, 2014.

[8] Maeda, H., Onodera, T., Nakayama, H., Inclusion complex of α-lipoic acid and modified cyclodextrins. *J Incl Phenom Macrocycl Chem* 68:201–206, 2010.

[9] Yallapu, M. M., Gupta, B. K., Jaggi, M., Chauhan, S. C., Fabrication of curcumin encapsulated PLGA nanoparticles for improved therapeutic effects in metastatic cancer cells. *J Colloid Interface* Sci, 351:19–29, 2010.

[10] Schittny, A., Huwyler, J., Puchkov, M., Mechanisms of increased bioavailability through amorphous solid dispersions: a review. *Drug Deliv,* 27:110–127, 2020.

[11] Dong, Y., Feng, S-S, Poly(d,l-lactide-co-glycolide)/montmorillonite nanoparticles for oral delivery of anticancer drugs. *Biomaterials,* 26:6068–6076, 2005.

[12] Cai, X., Riedl, B., Zhang, S. Y., Wan, H., The impact of the nature of nanofillers on the performance of wood polymer nanocomposites. *Compos Part A Appl Sci Manuf,* 39:727–737, 2008.

[13] Jawadi, Z., Yang, C., Haidar, Z. S., Santa Maria, P. L., Massa, S., Bio-Inspired Muco-Adhesive Polymers for Drug Delivery Applications. *Polymers (Basel),* 14:5459, 2022.

[14] Saltiel, A. R., Kahn, C. R., Insulin signalling and the regulation of glucose and lipid metabolism. *Nature,* 414:799–806, 2001.

[15] Roden, M., Price, T. B., Perseghin, G., Petersen, K. F., Rothman, D. L., Cline GW, Shulman GI, Mechanism of free fatty acid-induced insulin resistance in humans. *Journal of Clinical Investigation,* 97:2859–2865, 1996.

[16] Abay, A., Simionato, G., Chachanidze, R., Glutaraldehyde – A Subtle Tool in the Investigation of Healthy and Pathologic Red Blood Cells. *Front Physiol*, 2019. https://doi.org/10.3389/fphys.2019.00514

[17] Dong, Y., Feng, S-S, Poly(d,l-lactide-co-glycolide)/montmorillonite nanoparticles for oral delivery of anticancer drugs. *Biomaterials,* 26:6068–6076, 2005.

[18] Midaoui, A. EL., de Champlain, J., Prevention of Hypertension, Insulin Resistance, and Oxidative Stress by α-Lipoic Acid. *Hypertension,* 39:303–307, 2002.

[19] Lee, W. J., Song, K-H., Koh, E. H., Won, J. C., Kim, H. S., Park, H-S., Kim, M-S., Kim, S-W., Lee, K-U., Park, J-Y., α-Lipoic acid increases insulin sensitivity by activating AMPK in skeletal muscle. *Biochem Biophys Res Commun,* 332:885–891, 2005.

[20] Prabaharan, M., Mano, J. F., Chitosan-Based Particles as Controlled Drug Delivery Systems. *Drug Deliv,* 12:41–57, 2004.

[21] Oliveira, A. C. S., Ugucioni, J. C., Borges, S. V., Effect of glutaraldehyde/glycerol ratios on the properties of chitosan films. *J Food Process Preserv*, 2021. https://doi.org/10.1111/jfpp.15060

[22] George, A., Shrivastav, P. S., Preparation and evaluation of chitosan-alginate/carrageenan hydrogel for oral drug delivery in the treatment of diabetes. *J Bioact Compat Polym,* 38:368–386, 2023.

[23] Marapureddy, S. G., Thareja, P., Synergistic effect of chemical crosslinking and addition of graphene-oxide in Chitosan—Hydrogels, films, and drug delivery. *Mater Today Commun,* 31:103430, 2022.

[24] Fizir, M., Dramou, P., Dahiru, N. S., Ruya, W., Huang, T., He, H., Halloysite nanotubes in analytical sciences and in drug delivery: A review. *Microchimica Acta,* 185:389, 2018.

[25] Dzeikala, O., Prochon, M., Sedzikowska, N., Gelatine Blends Modified with Polysaccharides: A Potential Alternative to Non-Degradable Plastics. *Int J Mol Sci,* 25:4333, 2024.

[26] Idumah, C. I., Hassan, A., Ogbu, J., Ndem, J. U., Nwuzor, I. C., Recently emerging advancements in halloysite nanotubes polymer nanocomposites. *Compos Interfaces,* 26:751–824, 2019.

[27] Tipa, C., Cidade, M. T., Borges, J. P., Costa, L. C., Silva, J. C., Soares, P. I. P., Clay-Based Nanocomposite Hydrogels for Biomedical Applications: A Review. *Nanomaterials,* 12:3308, 2022.

[28] Tokarev, I., Minko, S., Stimuli-Responsive Porous Hydrogels at Interfaces for Molecular Filtration, Separation, Controlled Release, and Gating in Capsules and Membranes. *Advanced Materials,* 22:3446–3462, 2010.

[29] Das, M. P., R. S. P., Prasad, K., Jv V., M. R., Extraction and Characterization of Gelatin: A Functional Biopolymer. *Int J Pharm Pharm Sci,* 9:239, 2017.

[30] Campo, V. L., Kawano, D. F., Silva, D.B. da, Carvalho, I., Carrageenans: Biological properties, chemical modifications and structural analysis – A review. *Carbohydr Polym,* 77:167–180, 2009.

[31] Bigi, A., Cojazzi, G., Panzavolta, S., Rubini, K., Roveri, N., Mechanical and thermal properties of gelatin films at different degrees of glutaraldehyde crosslinking. *Biomaterials,* 22:763–768, 2001.

[32] Atyaksheva, L. F., Kasyanov, I. A., Halloysite, Natural Aluminosilicate Nanotubes: Structural Features and Adsorption Properties (A Review). *Petroleum Chemistry,* 61:932–950, 2021.

[33] Arnold, R., Azzam, W., Terfort, A., Wöll, C., Preparation, Modification, and Crystallinity of Aliphatic and Aromatic Carboxylic Acid Terminated Self-Assembled Monolayers. *Langmuir,* 18:3980–3992, 2002.

[34] Biddeci, G., Cavallaro, G., Di Blasi, F., Lazzara, G., Massaro, M., Milioto, S., Parisi, F., Riela, S., Spinelli, G., Halloysite nanotubes loaded with peppermint essential oil as filler for functional biopolymer film. *Carbohydr Polym,* 152:548–557, 2016.

[35] Yang, M., Wei, D., Mo, C., Zhang, J., Wang, X., Han, X., Wang, Z., Xiao, H., Saturated fatty acid palmitate-induced insulin resistance is accompanied with myotube loss and the impaired expression of health benefit myokine genes in C2C12 myotubes. *Lipids Health, Dis* 12:104, 2013.

[36] Listenberger, L. L., Han, X., Lewis, S. E., Cases, S., Farese, R. V., Ory, D. S., Schaffer, J. E., Triglyceride accumulation protects against fatty acid-induced lipotoxicity. *Proceedings of the National Academy of Sciences,* 100:3077–3082, 2003.

[37] Mikušová, V., Mikuš, P., Advances in Chitosan-Based Nanoparticles for Drug Delivery. *Int J Mol Sci,* 22:9652, 2021.

[38] Nelson, K. M., Dahlin, J. L., Bisson, J., Graham, J., Pauli, G. F., Walters, M. A., The Essential Medicinal Chemistry of Curcumin. *J Med Chem,* 60:1620–1637, 2017.

[39] Naumenko, E. A., Guryanov, I. D., Yendluri, R., Lvov, Y. M., Fakhrullin R. F., Clay nanotube–biopolymer composite scaffolds for tissue engineering. *Nanoscale,* 8:7257–7271, 2016.

[40] Naumenko, E., Fakhrullin, R., Halloysite Nanoclay/Biopolymers Composite Materials in Tissue Engineering. *Biotechnol J,* 2019. https://doi.org/10.1002/biot.201900055

[41] Iman, M., Maji, T. K., Effect of crosslinker and nanoclay on starch and jute fabric based green nanocomposites. *Carbohydr Polym,* 89:290–297, 2012.

[42] Hezaveh, H., Muhamad, II, Effect of MgO nanofillers on burst release reduction from hydrogel nanocomposites. *J Mater Sci Mater Med,* 24:1443–1453, 2013.

[43] Espitia, P. J. P., Soares, N de FF, Teófilo, R. F., Coimbra JS dos R, Vitor DM, Batista RA, Ferreira SO, de Andrade NJ, Medeiros EAA, Physical–

mechanical and antimicrobial properties of nanocomposite films with pediocin and ZnO nanoparticles. *Carbohydr Polym,* 94:199–208, 2013.

[44] Kasaai, M., A review of several reported procedures to determine the degree of N-acetylation for chitin and chitosan using infrared spectroscopy. *Carbohydr Polym,* 71:497–508, 2008.

[45] Campo, V. L., Kawano, D. F., Silva, DB da, Carvalho, I., Carrageenans: Biological properties, chemical modifications and structural analysis – A review. *Carbohydr Polym,* 77:167–180, 2009.

[46] Kotha, R. R., Luthria, D. L., Curcumin: Biological, Pharmaceutical, Nutraceutical, and Analytical Aspects. *Molecules,* 24:2930, 2019.

[47] Singh, N., Singh, P. K., Shukla, A., Singh, S., Tandon, P., Synthesis and Characterization of Nanostructured Magnesium Oxide: Insight from Solid-State Density Functional Theory Calculations. *J Inorg Organomet Polym Mater,* 26:1413–1420, 2016.

[48] Goy, R. C., Britto, D de, Assis, O.B.G., A review of the antimicrobial activity of chitosan. *Polímeros,* 19:241–247, 2009.

[49] Zocchi, M., Bartolini, M., Maier, J. A., Castiglioni, S., Low extracellular magnesium induces phenotypic and metabolic alterations in C2C12-derived myotubes. *Sci Rep,* 13:19425, 2023.

[50] Gojova, A., Guo, B., Kota, R. S., Rutledge, J. C., Kennedy, I. M., Barakat, A. I., Induction of Inflammation in Vascular Endothelial Cells by Metal Oxide Nanoparticles: Effect of Particle Composition. *Environ Health Perspect,* 115:403–409, 2007.

[51] Krishnamoorthy, K., Moon, J. Y., Hyun, H. B., Cho, S. K., Kim, S-J, Mechanistic investigation on the toxicity of MgO nanoparticles toward cancer cells. *J Mater Chem,* 22:24610, 2012.

[52] Gogoi, P., Das, M. K., Ramteke, A., Maji, T.K., Soy flour–ZnO nanoparticles for controlled release of silibinin: Effect of ZnO nanoparticle, surfactant, and cross-linker. *International Journal of Polymeric Materials and Polymeric Biomaterials,* 67:543–552, 2018.

[53] Lu, X., Shi, S., Li, H., Magnesium oxide-crosslinked low-swelling citrate-based mussel-inspired tissue adhesives. *Biomaterials,* 232:119719, 2020.

[54] Chen, J., Garcia, E. S., Zimmerman, S. C., Intramolecularly Cross-Linked Polymers: From Structure to Function with Applications as Artificial Antibodies and Artificial Enzymes. *Acc Chem Res,* 53:1244–1256, 2020.

[55] Paul, D. R., Robeson, L. M., Polymer nanotechnology: Nanocomposites. *Polymer (Guildf),* 49:3187–3204, 2008.

[56] Choi, J. H., Park, Y. W., Park, T. H., Song, E. H., Lee, H. J., Kim, H., Shin, S. J., Lau Chun Fai, V., Ju, B-K, Fuzzy Nanoassembly of Polyelectrolyte and Layered Clay Multicomposite toward a Reliable Gas Barrier. *Langmuir,* 28:6826–6831, 2012.

[57] Singh, J., Nayak, P., pH-responsive polymers for drug delivery: Trends and opportunities. *Journal of Polymer Science,* 61:2828–2850, 2023.

[58] Taourati, R., Khaddor, M., Laghzal, A., El Kasmi, A., Facile one-step synthesis of highly efficient single oxide nanoparticles for photocatalytic application. *Sci Afr,* 8:e00305, 2020.

[59] Paredes-Laverde, M., Montaño, D. F., Torres-Palma, R. A., Montmorillonite-Based Natural Adsorbent from Colombia for the Removal of Organic Pollutants from Water: Isotherms, Kinetics, Nature of Pollutants, and Matrix Effects. *Water (Basel)*, 15:1046, 2023.

[60] Eslah, F., Jonoobi, M., Faezipour, M., Afsharpour, M., Enayati, A. A., Preparation and development of a chemically modified bio-adhesive derived from soybean flour protein. *Int J Adhes Adhes*, 71:48–54, 2016.

[61] Iman, M., Maji, T. K., Effect of crosslinker and nanoclay on jute fabric reinforced soy flour green composite. *J Appl Polym Sci*, 127:3987–3996, 2013.

[62] Sampath Udeni Gunathilake, T. M., Ching, Y. C., Chuah, C. H., Illias, H. A., Ching, K. Y., Singh, R., Nai-Shang, L., Influence of a nonionic surfactant on curcumin delivery of nanocellulose reinforced chitosan hydrogel. *Int J Biol Macromol*,118:1055–1064, 2018.

[63] Almontasser, A., Parveen, A., Azam, A., Synthesis, Characterization and antibacterial activity of Magnesium Oxide (MgO) nanoparticles. *IOP Conf Ser Mater Sci Eng,* 577:012051, 2019.

[64] Xie, H., Ma, L., Li, Y., Fu, J., Li, Z., Yu, X., Gao, Q., Preparation and Characterizations of Curcumin Protection and Delivery System Using Linear Dextrin. *Compounds,* 2:353–366, 2022.

[65] Wu, X., Yang, Y., Research progress on drug delivery systems for curcumin in the treatment of gastrointestinal tumors. *World J Gastrointest Oncol,* 15:1342–1348, 2023.

[66] Gatou, M-A, Skylla, E., Dourou. P., Pippa, N., Gazouli, M., Lagopati, N., Pavlatou, E. A., Magnesium Oxide (MgO) Nanoparticles: Synthetic Strategies and Biomedical Applications. *Crystals (Basel),* 14:215, 2024.

[67] Li, D., Li, P., Xu, Y., Guo, W., Li, M., Chen, M., Wang, H., Lin, H., Progress in Montmorillonite Functionalized Artificial Bone Scaffolds: Intercalation and Interlocking, Nanoenhancement, and Controlled Drug Release. *J Nanomater*, 2022. https://doi.org/10.1155/2022/7900382

[68] Biswas, A., Nagaraja, A. T., You, Y-H., Roberts, J. R., McShane, M. J., Cross-linked nanofilms for tunable permeability control in a composite microdomain system. *RSC Adv,* 6:71781–71790, 2016.

[69] Aizawa, Y., Leipzig, N., Zahir, T., Shoichet, M., The effect of immobilized platelet derived growth factor AA on neural stem/progenitor cell differentiation on cell-adhesive hydrogels. *Biomaterials,* 29:4676–4683, 2008.

[70] Tian, H., Guo, G., Fu, X., Yao, Y., Yuan, L., Xiang, A., Fabrication, properties and applications of soy-protein-based materials: A review. *Int J Biol Macromol,* 120:475–490, 2018.

[71] Chauhan, S., Tomar, R. S., Unveiling the molecular networks underlying cellular impairment in Saccharomyces cerevisiae: investigating the effects of magnesium oxide nanoparticles on cell wall integrity and endoplasmic reticulum stress response. *Environmental Science and Pollution Research,* 31:30149–30162, 2024.